

JGR Solid Earth

RESEARCH ARTICLE

10.1029/2022JB024767

Key Points:

- Seafloor pressure records are coherent on the Alaskan shelf or slope, particularly within bathymetrically contiguous regions
- Exploiting coherence can reduce the root-mean-square error of de-tided seafloor pressure records up to 83% on the shelf and 93% on the slope
- Synthetic vertical motions of ≥ 4 cm on the shelf and ≥ 2 cm on the slope are detectable in 1-year seafloor pressure records

Supporting Information:

Supporting Information may be found in the online version of this article.

Correspondence to:

E. K. Fredrickson,
erikfred@uw.edu

Citation:

Fredrickson, E. K., Gomberg, J. S., Wilcock, W. S. D., Hautala, S. L., Hermann, A. J., & Johnson, H. P. (2023). Slow slip detectability in seafloor pressure records offshore Alaska.

Journal of Geophysical Research: Solid Earth, 128, e2022JB024767. <https://doi.org/10.1029/2022JB024767>

Received 12 MAY 2022

Accepted 25 JAN 2023

Author Contributions:

Conceptualization: Erik K. Fredrickson, Joan S. Gomberg, William S. D. Wilcock, Susan L. Hautala, Albert J. Hermann, H. Paul Johnson

Data curation: Erik K. Fredrickson, Joan S. Gomberg, Susan L. Hautala, Albert J. Hermann, H. Paul Johnson

Formal analysis: Erik K. Fredrickson

Investigation: Erik K. Fredrickson, Joan S. Gomberg

Methodology: Erik K. Fredrickson, Joan S. Gomberg, William S. D. Wilcock, Susan L. Hautala, Albert J. Hermann, H. Paul Johnson

Project Administration: H. Paul Johnson

Resources: William S. D. Wilcock

© 2023 American Geophysical Union.
All Rights Reserved. This article has been contributed to by U.S. Government employees and their work is in the public domain in the USA.

Slow Slip Detectability in Seafloor Pressure Records Offshore Alaska

Erik K. Fredrickson¹ , Joan S. Gomberg² , William S. D. Wilcock¹, Susan L. Hautala¹ , Albert J. Hermann^{3,4} , and H. Paul Johnson¹ 

¹School of Oceanography, University of Washington, WA, Seattle, USA, ²U.S. Geological Survey, WA, Seattle, USA, ³Joint Institute for the Study of the Atmosphere and Ocean, University of Washington, WA, Seattle, USA, ⁴NOAA Pacific Marine Environmental Laboratory, WA, Seattle, USA

Abstract In subduction zones worldwide, seafloor pressure data are used to observe tectonic deformation, particularly from megathrust earthquakes and slow slip events (SSEs). However, such measurements are also sensitive to oceanographic circulation-generated pressures over a range of frequencies that conflate with tectonic signals of interest. Using seafloor pressure and temperature data from the Alaska Amphibious Community Seismic Experiment, and sea surface height data from satellite altimetry, we evaluate the efficacy of various seasonal and oceanographic pressure signal proxy corrections and conduct synthetic tests to determine their impact on the timing and amplitude prediction of ramp-like signals typical of SSEs. We find that subtracting out the first mode of the complex empirical orthogonal functions of the pressure records on either the shelf or slope yields signal root-mean-square error (RMS) reductions up to 73% or 80%, respectively. Additional correction with proxies that exploit the depth-dependent spatial coherence of pressure records provides cumulative variance reductions up to 83% and 93%, respectively. Our detectability tests show that the timing and amplitude of synthetic SSE-like ramps can be well constrained for ramp amplitudes ≥ 4 cm on the shelf and ≥ 2 cm on the slope, using a fully automated detector. The principal limits on detectability are residual abrupt changes in pressure that occur as part of the transition to and from summer to winter conditions but are not adequately characterized by our seasonal corrections, as well as the inability to properly account for instrumental drift, which is not readily separated from the seasonal signal.

Plain Language Summary Our understanding of the world's largest and most damaging earthquakes mainly comes from land-based observations. However, the regions where these earthquakes are generated are predominantly located beneath the oceans, where observations are more limited and more difficult. Between large earthquakes, many processes occur that inform the behavior of these regions, such as "slow slip" events that are comparable to earthquakes but take place over weeks to months. Slow slip has recently been observed offshore using seafloor pressure sensors, which measure the weight of the overlying water and therefore record the changes in elevation caused by these events. A major limitation of pressure sensors is that they also record large signals caused by ocean circulation, which obscure seafloor elevation changes. In this study, we use pressure data from offshore Alaska to show that circulation-related signals can be reduced by as much as 93% by exploiting their similarity at comparable water depths over immense distances, making slow slip observation significantly easier. We confirm this with a detectability test on mock slow slip signals inserted into corrected pressure data, showing that we can detect signals as small as 4 cm in shallow water and as small as 2 cm in deep water.

1. Introduction

The world's largest faults, subduction zone plate-interfaces, are found mostly offshore. An increasing body of work has shown that the offshore segments of subduction faults slip both seismically in earthquakes and aseismically in transient slow slip events (SSEs) (Dixon et al., 2014; Ozawa et al., 2007; Radiguet et al., 2016; Ruiz et al., 2014; Vallée et al., 2013; Wallace & Beavan, 2010). In addition to adding to the global inventory of slow slip phenomena and understanding of their relation to tectonic environmental conditions, SSEs provide key constraints on slip that occurs as damaging earthquakes. Such implications have led to the increased use of absolute pressure gauges (APGs) to detect and measure vertical deformation caused by SSEs. However, a principal complication of these observations is that ocean circulation generates significant seafloor pressure signals that resemble, obscure, and/or interfere with potential geodetic signals. The need for approaches to reliably detect and

Supervision: Joan S. Gomberg, William S. D. Wilcock

Writing – original draft: Erik K. Fredrickson

Writing – review & editing: Erik K. Fredrickson, Joan S. Gomberg, William S. D. Wilcock

characterize SSEs in seafloor pressure records motivates this study and others (Fredrickson et al., 2019; Gomberg et al., 2019; He et al., 2020; Inoue et al., 2021; Muramoto et al., 2019; Woods et al., 2020).

Here, we focus on assessing the efficacy of various observational proxies to correct for the ocean circulation-generated component of bottom pressure, as quantified by variance reduction and by the ability to detect and characterize a suite of synthetic SSE deformation signals on a single station. We begin by providing a framework for our approach and noting that on the seafloor, APGs measure the change in the weight of the overlying water column that is due to changes in the sea surface height (SSH), water column density structure, and seafloor vertical position changes. In functional form, the measured seafloor pressure, P , may be considered as a linear combination of signals (e.g., Gomberg et al., 2019), denoted as:

$$P(x, t) = P_T + P_O + P_G + P_D + \epsilon$$

in which all terms vary with location, x , and time, t , and represent pressure changes due to ocean and Earth tides (P_T), non-tidal ocean circulation (P_O), geodetic deformation (P_G), instrumental drift (P_D), and unmodeled signal (ϵ). Herein, we are concerned with isolating and reliably characterizing P_G , specifically for the case of offshore SSE deformation. A first-order functional representation of P_G is a ramp with amplitude of 1.5–6 hPa and rise-times of 1–4 weeks, observed over regions of 40–80 km diameter (Davis et al., 2015; Ito et al., 2013; Wallace et al., 2016), though only a limited number of offshore SSEs have been observed to date. 1 hPa is roughly equal to 1 cm of water column height, and herein we use cm.

P_T is the largest of the component terms in most observations, on the order of 10² cm and variable with location, but is readily removed with standard methods, including low-pass filtering or fitting with a tidal model (e.g., Foreman et al., 2000; Polster et al., 2009). P_D for the most precise and widely used APGs is reasonably characterized as a combined exponential and linear trend (Polster et al., 2009) but both terms are unpredictable before deployment. P_D is typically accounted for by least-squares fitting with the assumed functional form, or by removing the first month(s) of data and assuming purely linear drift thereafter. Thus, this signal is particularly problematic for deployments with relatively short durations of months to a year, as is typical of most large-scale deployments to date (e.g., Barchek et al., 2020; Todd et al., 2018; Toomey et al., 2014). P_O contains a complex suite of signals, with variations typically exceeding those of P_G , including seasonal variation, oscillatory effects such as seasonal fluctuations and weather band energy (periods of 5–14 days), and stochastic processes that include meso-scale eddies and coastal trapped waves (e.g., Hughes et al., 2018; Wang & Mooers, 1976). While oscillatory signals in P_O are theoretically distinguishable from the non-oscillatory P_G , even in the absence of any explicit knowledge of the local circulation, the typical limited duration of seafloor pressure time series complicates this distinction.

The traditional proxy for P_O is a reference pressure, P_{ref} , recorded close to the trench on the incoming plate and assumed to be representative of the network oceanographic pressure fluctuations and to contain no deformation signal. This proxy has been used in the Japan Trench by Ito et al. (2013) and in Hikurangi by Wallace et al. (2016) to identify SSE deformation signals. The assumptions inherent in P_{ref} are broadly consistent with the current state of knowledge of seafloor pressure from physical oceanography on the time-scales important to SSE detection. For example, Hughes et al. (2018) demonstrated with a global ocean model the coherence of seafloor pressure throughout the entire Atlantic basin at nominal continental slope depths of 100–3,200 m. Additionally, for periods of several days to about 2 weeks, the ocean response is largely barotropic (i.e., depth-independent) with spatial coherence over 1,000 km scales, reflecting the footprint of atmospheric forcing in the so-called “weather band” (Luther et al., 1990). Recent work in Cascadia and Hikurangi has demonstrated that P_{ref} has mixed effectiveness that depends on the network geometry and performs particularly poorly on the shelf (Fredrickson et al., 2019; Gomberg et al., 2019; Inoue et al., 2021).

Another proxy that also relies on the spatial coherence of the ocean-generated pressure field—in this case, expected along-margin coherence (Hughes & Meredith, 2006)—uses a pressure record at a site far from the posited SSE deformation at approximately the same depth (i.e., “depth-matched”), independently selected for each station. We refer to this proxy as P_{match} . This approach was suggested by Fredrickson et al. (2019) from work in Cascadia and confirmed to work well in Hikurangi by Inoue et al. (2021). Both studies demonstrated that for strict depth matching criteria (tens of meters) on the shelf and much more lenient matching on the lower slope and abyssal plain, P_{match} is capable of reducing signal root-mean-square error (RMS) amplitude to better than 1 cm, over station separations of hundreds of kilometers in Cascadia, and at least 80 km in Hikurangi where instruments

were deployed over a much smaller region. Previously observed shallow SSEs (Araki et al., 2017; Ito et al., 2013; Wallace et al., 2016) and the forward modeling of Fredrickson et al. (2019) show that SSEs of $M_w < 7.0$ generally produce deformation fields with dimensions smaller than 100 km, and therefore P_{match} should be effective if it is selected from distances beyond likely SSE dimensions.

The spatial coherence of the seafloor pressure field may also be exploited using complex empirical orthogonal functions (CEOFs) (e.g., Thomson & Emery, 2014), which capture not only the synchronously coherent component of the pressure field, but also allow for propagating oceanographic signals; effectively a CEOF decomposition is a principal component analysis that allows for phase-shifts between input signals. CEOFs have previously been used in Cascadia to derive a correction for seasonal and non-seasonal P_o signals (Watts et al., 2021) and comparable principal component analysis has been used to analyze megathrust earthquake deformation recorded by bottom pressure sensors during the 2011 Tohoku-Oki event (Hino et al., 2014). In the context of this study, we refer to the first CEOF as a seasonal correction, but recognize that it captures higher frequency features as well. Herein, we derive CEOFs from a collection of contemporaneous seafloor pressure records and we can assume that oceanographic signals dominate the first mode because it captures the lowest frequency pattern that is shared among the greatest number of stations. CEOFs derived from combined records of pressure and other data types that are sensitive to the same oceanographic processes, or multivariate CEOFs, also may be used. The inclusion of additional data that are insensitive to geodetic deformation may reduce the potential for it to be represented in the CEOFs and eliminated when applied as a proxy.

Non-pressure observables measured on co-located sensors have been used as proxies for ocean pressures, and benefit from not relying on spatial coherence assumptions. Hydrostatic pressure at the seafloor is related to both SSH and integrated water column density variations, although information about the latter is typically limited to seafloor temperature. Baba et al. (2006), Gomberg et al. (2019), and Itoh et al. (2019) examined correlations between seafloor pressure and temperature in the Japan and Hikurangi subduction zones. Assuming a linear relationship between pressure and temperature fluctuations, as well as negligible influence on the temperature field by tectonic deformation, the proxy P_{temp} can be constructed from scaled and possibly time-lagged temperatures. Likewise, the correlation between SSH and bottom pressure is well-documented, particularly in shallow water (e.g., Siegmund et al., 2011), but to our knowledge, this has never been used in the study of offshore tectonic processes. However, in deeper locations, water column structure acts to compensate pressure perturbations caused by changing SSH (e.g., Dobashi & Inazu, 2021) and so we hypothesize P_{SSH} to be more effective on the shelf than on the slope and abyss. Similarly, previous studies (Dobashi & Inazu, 2021; Fredrickson et al., 2019; Inoue et al., 2021; Muramoto et al., 2019) have constructed proxies from collocated hindcasts of seafloor pressure from numerical models of oceanographic circulation but have shown that such simulations are not accurate enough to provide useful corrections.

In this study, we use observations from the Alaska margin to systematically compare pressure correction techniques for minimizing the instrumental and oceanographic components of $P(x,t)$ in an oceanographically challenging setting and evaluate the detectability of synthetic single-station SSE signals in these corrected data. Although subtle evidence for a single SSE in the same pressure data has been reported by He et al. (2021), these pressure data are clearly dominated by oceanographic signals and thus suitable for a study that compares various techniques for assessing the detectability of synthetic signals for various processing approaches.

2. Geologic and Oceanographic Setting

This study focuses on the Alaska Peninsula Subduction Zone (Figure 1), where the Pacific Plate subducts beneath the North American Plate, which has historically hosted numerous large megathrust earthquakes. This region was the focus area for the 2018–2019 Alaska Amphibious Community Seismic Experiment (AACSE), which was aimed at understanding along-strike variability in geodetic and seismic deformation processes, through seismic and geodetic (APG) observation and subsurface structural imaging (Abers et al., 2019; Barchek et al., 2020). Within this footprint, the region roughly between 158° and 161° W, known as the Shumagin gap, had not ruptured in an $M_w > 8.0$ earthquake within the period of instrumental records (Davies et al., 1981). The available onshore data suggest this segment is weakly locked and is presumed to accommodate a significant fraction of plate convergence aseismically, though resolution near the trench is poor (Fournier & Freymueller, 2007; Li & Freymueller, 2018). Recently, in July and October of 2020, the gap was partially ruptured by two $M_w > 7.5$ earthquakes (Crowell & Melgar, 2020), and in July of 2021, an $M_w 8.2$ earthquake occurred just east of the gap,

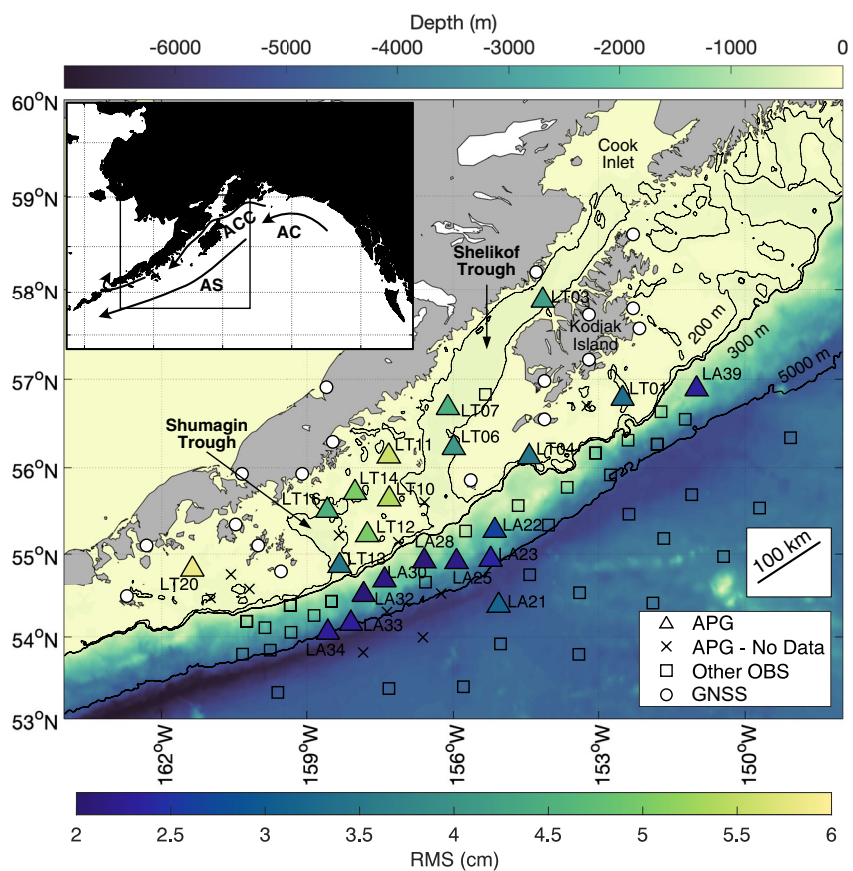


Figure 1. Map of the experiment area offshore the Alaska Peninsula. Filled triangles indicate the absolute pressure gauges (APGs) used in this study, colored by the root-mean-square error (RMS) of their tidally filtered, drift-corrected data. “X” markers indicate APGs that did not return data. Square markers indicate other OBS from the AACSE in the region and circles indicate proximal GNSS stations active during the AACSE deployment. Bold depth contours at 300 and 5,000 m approximate the shelf break and trench, respectively. Inset shows broader geographic context and major circulation features. AC, Alaska Current; ACC, Alaska Coastal Current; AS, Alaska Stream.

likely triggered by the previous year's events (Elliott et al., 2022). Although this subduction zone has hosted several documented SSEs and tremor episodes down dip of the seismogenic zone (Brown et al., 2013; Li & Freymueller, 2018; Rousset et al., 2019); to date, there is only limited evidence for SSEs within or up dip of the seismogenic zone (He et al., 2021).

In addition to the barotropic weather band response highlighted earlier, ocean circulation has a significant effect on seafloor pressure, and here, we summarize some of its distinguishing features offshore of Alaska. On a gross scale, the circulation is dominated by the Alaska Current, a boundary current at the northern rim of the counter-clockwise Pacific subarctic gyre (Figure 1 inset). Following the geography of the Alaska Peninsula, the Alaska Current narrows to ~50 km and strengthens, becoming a western boundary current: the Alaskan Stream. The Alaskan Stream extends to depths >3,000 m and flows southwest along the lower continental slope, overlying a deep northeastward current directly along the Alaska Trench (Warren & Owens, 1988). Changes in wind-forced subarctic Ekman pumping affect regional sea level patterns and the strength of the Alaskan Stream (Capotondi et al., 2009), which is in geostrophic balance with the cross-stream pressure gradient—the along-stream pressure gradient being much weaker. Relatively strong mesoscale (~100 km) variability occurs, consistent with its dynamics as a western boundary current. These shifts in the intensity and location of the Alaskan Stream relative to the slope, on the timescales of several weeks to several months (Reed & Stabeno, 1989), are expected to lead to coherent pressure changes at the seafloor. This region is also characterized by coastally trapped waves that propagate southwestward along the slope associated with locally and remotely forced SSH variations on time scales ranging from weeks to years (Hermann et al., 2009) and that propagate pressure variations efficiently along isobaths. Thus, for a wide range of time scales relevant to the detection of SSEs, we expect pressure signals

on the lower slope to show coherence along isobaths, as observed in Cascadia by Fredrickson et al. (2019) and in Hikurangi by Inoue et al. (2021). A large part of the mesoscale variability in the Alaskan Stream is due to baroclinic eddies propagating to the southwest at speeds of a few km/day (Ladd et al., 2007), which may interrupt along-slope coherence or introduce lags, although the depth of penetration of associated pressure anomalies is uncertain.

Ocean circulation on the shelf and coast is dominated by the Alaska Coastal Current but is less organized than further offshore, being affected by significant freshwater input, flows strongly steered by regional-scale bathymetric features, and wind forcing that can lead to daily averaged surface currents that may exceed 100 cm/s (Stabeno, Bond, et al., 2016). Onshore/offshore Ekman transport that rapidly adjusts to changes in the along-shore wind leads to significant SSH changes over the shelf (Capotondi et al., 2009). All these factors lead to larger, less spatiotemporally coherent seafloor pressure variations and most geodetic studies elsewhere have simply avoided incorporating shelf observations. However, avoiding the shelf offshore of Alaska would make most of the AACSE's geodetic goals unachievable, given the ~150 km width of the shelf.

In summary, oceanographic signals related to both tidal and non-tidal processes are large offshore of the Alaska Peninsula. The array of non-tidal processes includes the high rate of meso-scale (~100 km diameter) eddies generated both locally and propagating in from the eastern Gulf of Alaska (Ladd et al., 2007; Reed & Stabeno, 1989), the presence of strong wind-driven boundary currents that extend over the shelf and continental slope (Stabeno, Bell, et al., 2016), complex bottom topography, strong storms, seasonal cycles (that tend to be stronger in the west), laterally meandering currents and eddies, upwelling and downwelling (Stabeno et al., 2004), the variable strength and cross-slope location of the Alaska Stream (Stabeno & Hristova, 2014), and abyssal boundary currents (Warren & Owens, 1988). Thus, we anticipate that oceanographic corrections for pressure geodesy may be particularly challenging in this setting.

At the same time, seafloor pressure observations are sparse, not just in Alaska but globally and extrapolation is limited by the immense range of spatial and temporal scales involved in ocean circulation (e.g., Wunsch, 2016). The circulation processes described above are expected to influence the bottom pressure field but have not been comprehensively studied or verified observationally, particularly those that have been invoked to affect pressure on the ~100 km scale.

Despite these challenges, our preliminary explorations indicate that regional ocean model hindcasts of the northern Gulf, forced with observed atmospheric conditions but assimilating no ocean data internally (e.g., Coyle et al., 2019, extended through the time period of this study), can faithfully reproduce some of the large-scale, wind-forced pressure variations associated with upwelling/downwelling and coastal-trapped wave signals on the shelf and upper slope. However, in the absence of dense oceanic data simulation, a much weaker correspondence with pressure variations is observed on the lower slope, partly due to the inevitable model/data mismatch in the timing and location of the (fundamentally chaotic, nonlinear) mesoscale eddies and current meanders—with ~100-km length and weekly to several month time scales—which populate the Alaskan Stream region. Further, even where greater correspondence is seen on the shelf, these model hindcasts do not capture a significant portion of the finer-scale spatiotemporal variability in the observational data.

3. Methods

3.1. Pressure, Temperature, and Altimetry Data

The pressure and temperature data used in this study come from the offshore component of the AACSE (see Data Availability Statement section), which included 75 ocean-bottom instrument packages deployed for 15 months from May 2018 through September 2019, roughly between Kodiak and the Shumagin Islands, from the near-shore out to the abyssal plain. About 35 of the AACSE instruments were equipped with Paroscientific APGs, and of these, 25 were recovered and yielded usable data for this study (Figure 1). Of these, three sensors stopped recording midway through the deployment and are excluded from this study for the sake of consistency between records in our analysis. Thus, we present pressure data from each of the 9 slope sites (depth \geq 1,564 m), 12 shelf sites (depth \leq 262 m), and 1 site on the incoming plate. Note that between network design and failed instrument recoveries, no seafloor data were available for this study for depths between 262 and 1,564 m. A combination of Antares, Star-Oddi DST CTD, and HOBO TidbiT temperature loggers was attached externally to many of the AACSE instruments and returned data for all but two of the pressure-recording instruments used in this study.

For these two instruments (LA21 and LA28), data from the internal temperature sensor of the Paroscientific APG were used instead. Time series of SSH were obtained for all station locations, compiled as a Jason-3 satellite product by the Copernicus Program (Taburet et al., 2019; see Data Availability Statement section). All data were truncated as necessary so that all time series were of the same duration, beginning on June 8, 2018, and ending on June 20, 2019, for a duration of 377 days.

As our interest lies in signals with periods of a few days or longer, we down-sample the pressure and temperature data to 1 sample/hr and apply a 24–24–25 Godin lowpass “tide-elimination” filter (Thomson & Emery, 2014). The SSH data are provided at a daily sample rate pre-corrected for tides. Throughout this study, we separate the data into shelf and slope groupings, based on the coherence of data in each that is apparent visually, and consistent with previous studies (e.g., Fredrickson et al., 2019; Wallace et al., 2016), water column dynamics (Hughes & Meredith, 2006), and corroborated in this study.

3.2. Corrections to Remove Non-Tectonic Long-Period Signals

The instrumental drift, P_D , is unique to each sensor and in some cases may be as large or larger than the seasonal variation. For all our analyses, we solve for P_D using a least-squares inversion, linearized by solving repeatedly assuming exponential time constants ranging from 1 day to 6 months. Nonlinear sensor drift was not generally apparent in the temperature data, evidenced by comparing temperature records from the sites with multiple different temperature sensor types, and only linear trends were fit and subtracted from them. We assumed there was no drift in the SSH data, which were also given only a linear correction. The tidally filtered, drift-corrected data are shown in Figures 2a–2c for shelf instruments and in Figures 2d–2f for slope and abyss instruments.

As seen in other studies, the AACSE data exhibit a spatially variable seasonal signal. This is a component of P_O but we treat it separately as part of our processing. This seasonal signal can obscure SSE deformation signals, if present, and we explored several methods for removing it. First, we tested fitting two separate functional forms, a sinusoid (365.25 day period) and a third order polynomial—conducting all analyses for both alternatives to assess robustness. Though there is inherent risk in aliasing and removing some of P_G with these functional-form corrections, the fits determined for the AACSE pressures are modest in amplitude so any such effect is expected to be small (Figure S1 in Supporting Information S1). The sinusoidally and polynomially corrected data exhibit variability in individual time series, but do not produce substantially different results in aggregate. So, in the main text, we present and discuss only the sinusoidal results, while the polynomial equivalents are provided in the Supplementary Materials. A representative subset of the tidally filtered, drift-corrected, and sinusoidally corrected pressure data from the shelf is shown in blue in Figure 3a, with all data shown in Figures S2a (shelf) and S3a (slope and abyss) in Supporting Information S1. We also tested using two forms of corrections calculated from CEOFs, which are the complex principal components of Hilbert-transformed input data (see Thomson and Emery (2014) for details). One of these corrections is the first CEOF of the combined pressure data on either the shelf or slope, which we will refer to as the pressure-CEOFOF (p-CEOFOF). Similar CEOFs may be derived for the temperature or SSH data, and the first CEOFs for each data type are shown in red in Figure 2. As seen in the figure, the largest fluctuations in the first CEOFs are generally the seasonal fluctuations, but significant higher frequency content is also represented. The other correction considered is the first CEOF of the combined data set of pressure, temperature, and SSH data, again for either the shelf or slope. We refer to this as the multivariate-CEOFOF (m-CEOFOF) and we explore it because of the visually apparent, though complex relationships between the pressure, temperature, and SSH data. In either case, the CEOFs are sensitive to whatever signals contribute the greatest variance across all input data and thus are inherently insensitive to site-specific signals. In particular, incorporating P_G into the first CEOFOF is of the greatest concern for this study, but the dispersed network geometry and expected spatial scales of SSE deformation limit the possibility of capturing P_G on more than one or two sensors. Further mitigation is provided by the multivariate approach since deformation has no expression in temperature and SSH observations. Ultimately, the pressure-CEOFOF method outperformed the multivariate-CEOFOF method, so we present only the prior in the main text and show equivalent results for the latter in Figures S4, S6, and S8 in Supporting Information S1.

3.3. Proxies for Oceanographic Pressure, P_O

We explored a range of proxies for correcting the non-seasonal components of P_O , the first class of which are those derived from observations of pressure at other locations. Such pressure-derived proxies assume that P_O

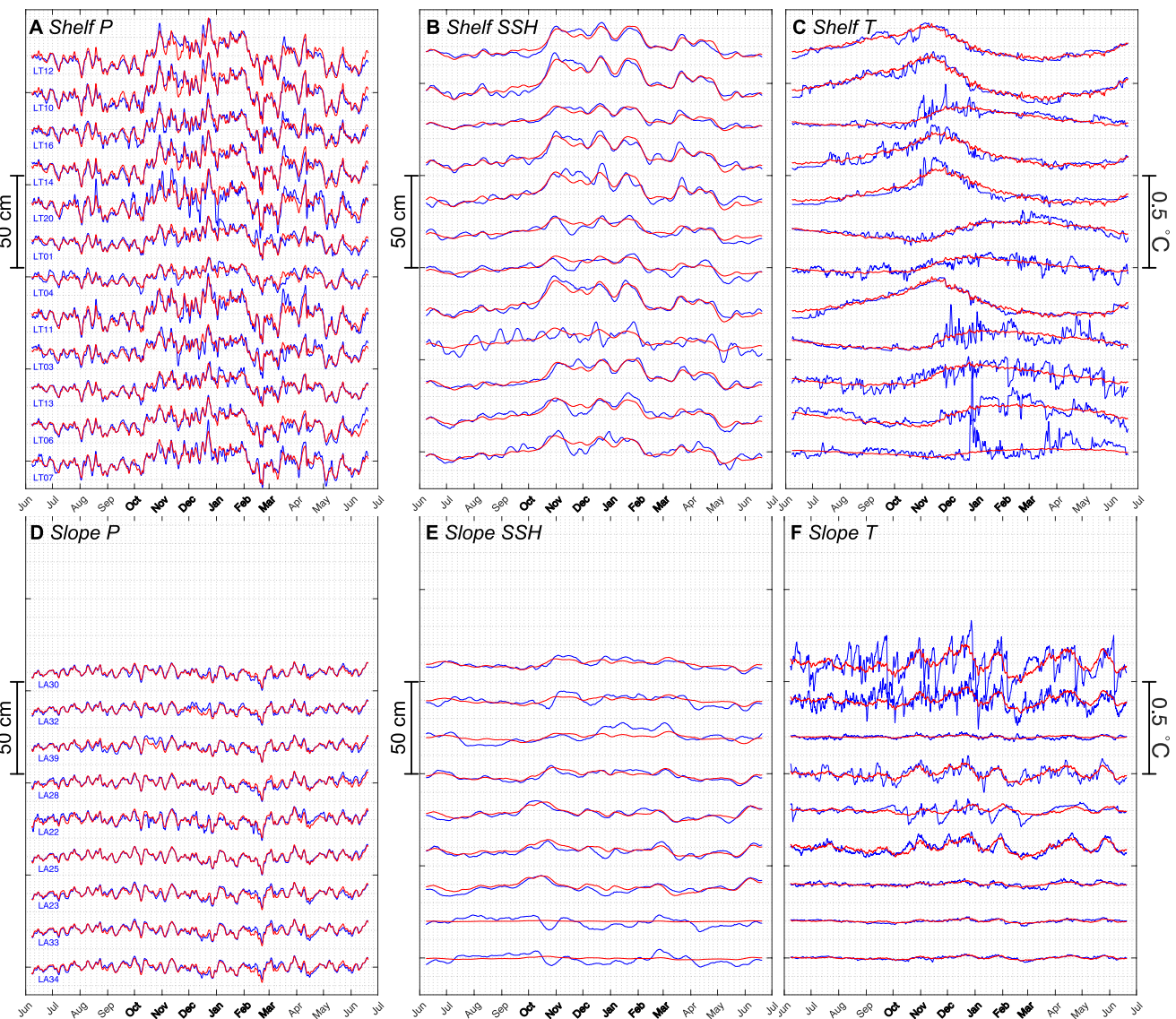


Figure 2. Time series of tidally filtered, drift corrected pressure, tidally filtered sea surface height (SSH), and tidally filtered temperature (blue), along with corresponding first pressure-complex empirical orthogonal function (CEOOF), SSH-CEOOF, and temperature-CEOOF (red), vertically offset with shallowest station at the top for display purposes. Winter months, when signals are anomalously large across observables, are labeled in bold. (a) Shelf pressure. (b) Shelf SSH. (c) Shelf temperature. (d) Slope pressure. (e) Slope SSH. (f) Slope temperature.

is coherent over spatial scales at least the size of the network—or subnetwork—being considered. Further, to avoid removing any or all of P_G when the proxy is applied, the coherent region must be larger than the region affected by an SSE. Only a single APG, LT21, was placed seaward of the trench and is therefore used as the incoming plate reference pressure, P_{ref} for all other sites (red curves, Figure 3b, Figures S2b and S3b in Supporting Information S1). Depth match station pairs, P_{match} (red curves, Figure 3c, Figures S2c and S3c in Supporting Information S1), were determined empirically, choosing the proxy pressures yielding the smallest signal RMS and separated by >80 km where possible and >50 km otherwise (Tables S1 and S2 in Supporting Information S1—list pair RMS values), to avoid subtracting out any potential common P_G signal. Given the limitations of working with a network of finite size, there were inherently tradeoffs between optimizing depth differences and separations. Further, we chose to avoid repeat station pairs (e.g., LT04-LT01 and LT01-LT04) when a comparably effective station pair was available to demonstrate the robustness of the method. Finally, we use a sub-network average pressure, P_{avg} , which we derive by normalizing each pressure record by its RMS and calculating an average. Though no spatial limitations comparable to those of P_{match} were used in the calculation of P_{avg} , this method

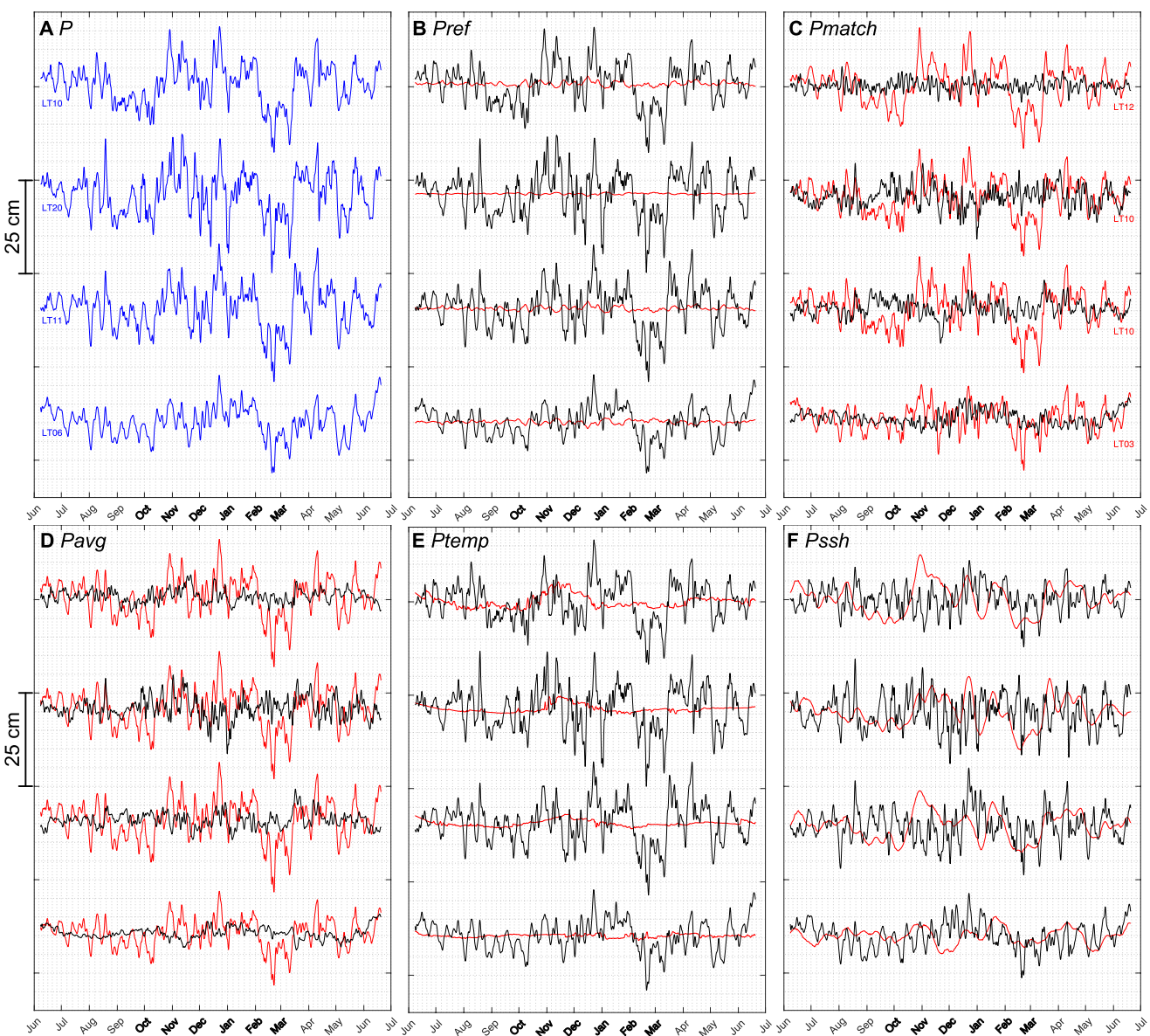


Figure 3. Time series of a representative subset of tidally filtered, drift and sinusoidal-corrected shelf pressure data (blue), scaled proxies (red), and proxy-corrected data (black), vertically offset with shallowest station at the top for display purposes. Winter months, when signals are anomalously large across observables, are labeled in bold. (a) No proxy. (b) Reference station pressure (P_{ref}). (c) Depth-matched pressure (P_{match}), with matched station labeled in red text. (d) Network average pressure (P_{avg}). (e) Temperatures, lagged to maximize correlation (P_{temp}). (f) Sea surface height (P_{SSH}).

is inherently less susceptible to contamination by common Pg signals since it will be scaled by the number of stations and since the majority of the network falls outside any expected deformation area. A separate P_{avg} is calculated for each of the shelf and slope regions (red curves, Figure 3d, Figures S2d and S3d in Supporting Information S1).

The second class of proxies is derived from independent, collocated measurements of ocean properties that respond to the same forces that drive the pressure changes, or are driven by the pressure gradients themselves, but that are not affected by SSE deformation. These proxies are derived from bottom temperatures (P_{temp} , red curves, Figure 3e, Figures S2e and S3e in Supporting Information S1), and from SSH (P_{SSH} , red curves, Figure 3f, Figures S2f and S3f in Supporting Information S1) recorded at or above each instrument site.

All proxies are applied as corrections by scaling to achieve best fit and subtracting them from the pressure record of interest to achieve the lowest RMS difference. We justify this scaling even for the P_{ref} and P_{match} proxies since

oceanographic pressure signals are known to scale with depth and may also be influenced by other local factors. The scale factors for P_{ref} varied from 0.72 to 1.04 on the shelf and from 0.84 to 1.11 on the slope, while those for P_{match} varied from 0.03 to 0.2 on the shelf and from 0.34 to 0.58 on the slope. P_{temp} was also lagged to account for delayed advective and wave adjustment of the density field and to achieve the highest correlation. We assume that temperature should always lag pressure because changing seafloor pressure gradients should drive bottom currents, tracked by their temperature signatures. However, since such gradients could result in the advection of either warmer or colder water, we search for the maximum absolute correlation. We also limited the lag to a 30-day maximum, with the optimal lags ranging from 7 to 24 days and generally being larger on the shelf than on the slope. We ascribe no physical meaning to the variation in these lags in terms of circulation processes, as the relationship between seafloor pressure and temperature is demonstrably complex. Lagging was unnecessary for all other proxies.

3.4. Synthetic SSE Detection and Characterization

We assessed the efficacy of the candidate proxies to improve the detection and characterization of possible SSEs by adding synthetic deformation signals to the tidally filtered (but otherwise unprocessed) AACSE pressures and quantifying the accuracy with which those signals' onset times and amplitudes were estimated with each type of seasonal and proxy correction. We perform our analyses in the absence of, and then assuming, known SSE onset timing to evaluate the benefit of independent information about events (e.g., from onshore GNSS data). Unlike other synthetic detectability studies for offshore deformation (e.g., Agata et al., 2019; Ariyoshi et al., 2014; Fredrickson et al., 2019), this analysis focuses on evaluating the detection threshold of an observed signal rather than assuming one and assessing the slip scenarios that could generate such signals.

Representative SSE deformation transients were generated as simple ramps with amplitudes ranging from 0 to 10 cm and durations ranging from 1 to 90 days so as to include the SSE characteristics observed elsewhere as well as to explore end member cases. Weekly onset times ranged from July 8, 2018, to May 19, 2019, which intentionally excluded the first and last 30 days of data (out of 377 days total) to reduce complications near the edges. For each amplitude considered, the duration was held at 14 days and for each duration considered the amplitude was fixed at 8 cm for shelf sites and 6 cm for slope sites, to assess the effect of duration on a large, readily detectable signal. The full range of onset times was used for every amplitude/duration combination to minimize any bias resulting from either positive or negative coherence of concurrent oceanographic signals with the synthetic ramp. Synthetics were added to only one pressure record at a time, then those modified data were put through the detrending and seasonal correction processing described above before attempting detection under the various proxy corrections. On the shelf, this analysis yielded 552 detection results per amplitude or duration per proxy (12 stations and 46 onsets considered) and on the slope it yielded 414 (9 stations and 46 onsets considered).

We opted for a fully automated approach to detect and characterize ramps to ensure the comparability of results between methods (Figure 4). For sinusoidal and polynomial seasonal corrections, the onset of an event was estimated by iteratively inverting, for every time step, the best-fit seasonal correction while allowing for an instantaneous offset in pressure at that time. We considered the time that yielded the lowest post-correction RMS value to indicate the center of the ramp. For the case of assumed known event onset, this step was unnecessary. To estimate the ramp amplitude, we then masked the 7 days before and after the estimated onset (for 14 days total) and re-inverted for the seasonal fit, again allowing for an offset in pressure on either side of the masked time period and considering that offset as equal to the ramp amplitude.

For the CEOF-based seasonal corrections, we endeavored to estimate the event onset similarly; however, the CEOF calculation does not allow for undefined offsets, unlike the inversions described above. Instead, at each time step, we inverted the CEOF corrected pressure for a linear fit with arbitrary offset at that time and again used the lowest RMS residual to determine the center of the ramp. In estimating the amplitude, we likewise endeavored to mirror the sinusoidal/polynomial scheme to the extent possible, given that the CEOF calculation does not allow for masking, while also recognizing that the presence of the synthetic ramp contaminated the CEOF calculation and could then lead to its partial or entire removal. Instead, for the determined (or assumed) onset time, we iteratively recalculated the CEOFs after subtracting out a 14-day ramp of variable amplitude from -20 to 20 cm. The CEOFs that yielded the lowest post-correction RMS value were then considered to be uncontaminated by the presence of the ramp and were used as a replacement seasonal correction for the original input data (i.e., those for which no attempt to subtract out the ramp had been made). Finally, to estimate the ramp amplitude

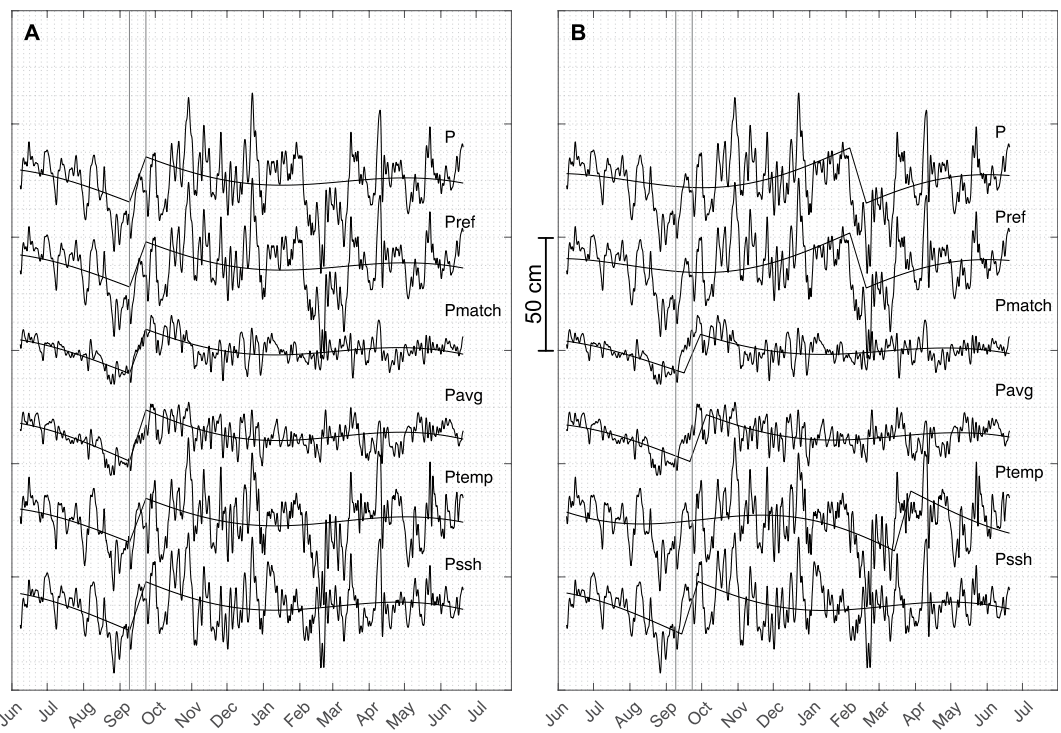


Figure 4. Demonstration of slow slip event signal detector for a 10 cm, 14-day ramp beginning on September 9, 2018 applied to sinusoidally corrected and proxy-corrected pressure records from station LT16 for (a) the case of known onset and (b) unknown onset. Each proxy-corrected time series is offset vertically for display purposes, from top to bottom: none, P_{ref} , P_{match} , P_{avg} , P_{temp} , and P_{ssh} . The vertical lines indicate the true synthetic event duration. Thin black curves show where the detector identifies the event and how it is characterized.

by the same method as the polynomial and sinusoidal cases, the newly CEOF-corrected data were masked for the 7 days before and after the estimated onset (for 14 days total) and inverted for a linear fit, again allowing for an offset in pressure on either side of the masked time period, with the offset considered to be the ramp amplitude.

4. Results

4.1. Seafloor Pressure Characteristics

Tidally filtered pressure data from the AACSE for the period of June 8, 2018, to June 20, 2019 (377 days) show complex residual oceanographic signals of varying amplitude. After filtering out the tides, correcting for sensor drift, and detrending (Figure 2a, Figures S2a and S3a in Supporting Information S1), signal amplitudes are seen to broadly scale inversely with station depth, decreasing from the continental shelf to the continental slope and abyssal plain (Figure 1). There is little variation in the signal amplitudes of the slope pressures despite the depth range of 1,564–4,612 m, for which signal RMS varies from 2.2 to 2.9 cm. The pressure record from the deepest instrument, LA21 (5,113 m) on the incoming Pacific Plate, has a notably larger RMS of 3.6 cm. Greater variability is seen on the shelf, where signal amplitudes do not vary systematically over the depth range of 83–262 m, but instead relate to broad-scale bathymetric features (Figure 1). Pressure RMS is lowest near the shelf break, at 3.7–4.3 cm, increasing to 4.7–5.2 cm within the Shelikof and Shumagin Troughs, and largest at the bathymetric high between the Shelikof and Shumagin Troughs and the one location west of the Shumagin Islands (LT20), at 6.2–6.9 cm. Despite these amplitude differences, the pressure data are remarkably coherent within the shelf and slope groupings, over separations of hundreds of kilometers, at both short and long periods (Figure 2a, Figures S2a and S3a in Supporting Information S1). This is particularly striking at periods of a few weeks or less, where pressures are not only coherent but synchronous within the hourly sample rate considered here, suggesting a barotropic response that is corroborated by the visual coherence between pressure and SSH (Figures 2b and 2e).

This domain-wide coherence in bottom pressure results in non-uniqueness in determining the proxy P_{match} . Figure 5 and Table S1 in Supporting Information S1 consider every combination of scaled station pair differences

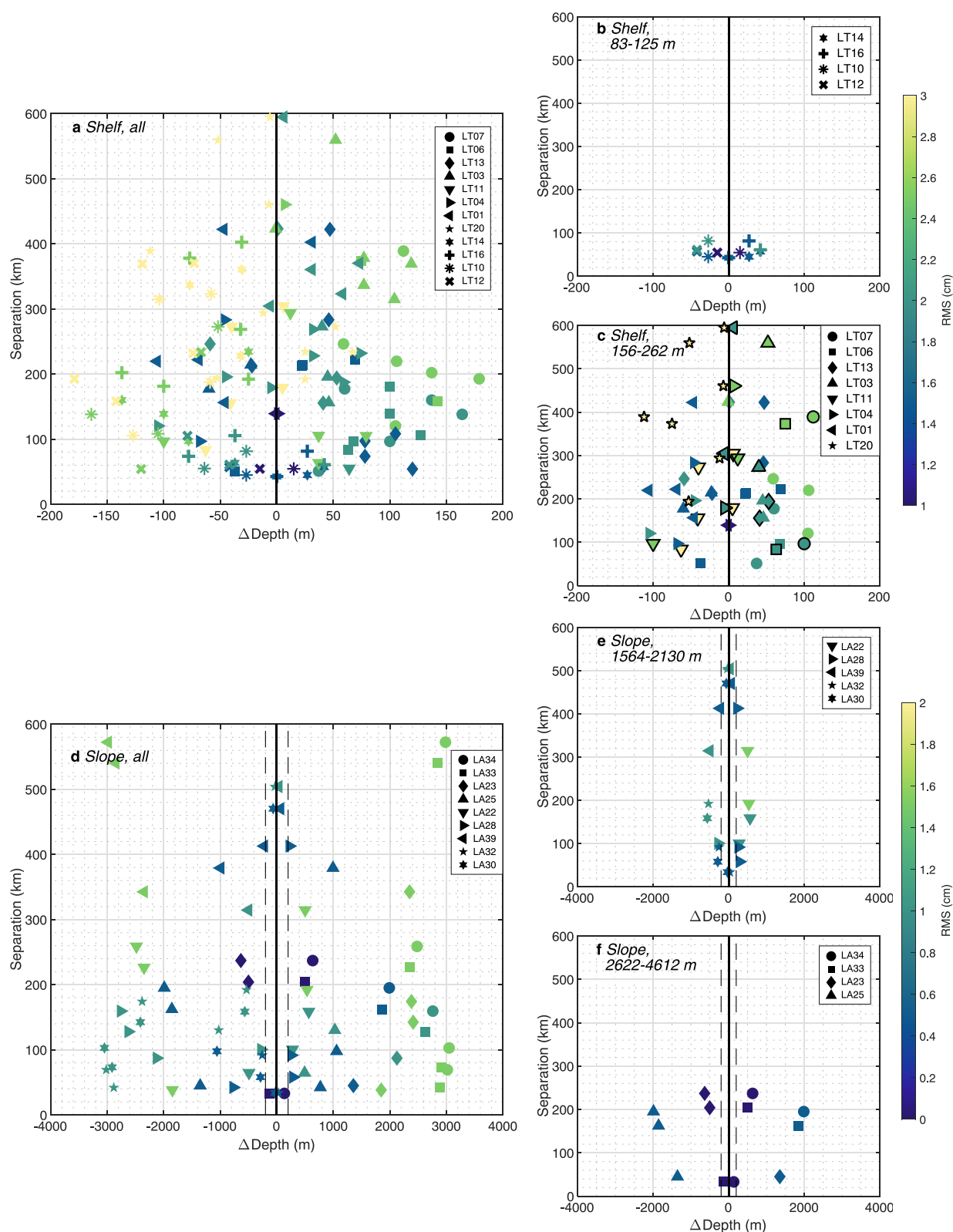


Figure 5.

within the shelf and slope groupings. We do this for sinusoidally corrected pressure data, with the aim of assessing signal similarity without drift, tidal, or seasonal signals, but before any proxy correction. Note that we consider symmetric differences (e.g., LT01–LT04 and LT04–LT01) and that because of the scaling described in Section 3.3, these do not necessarily yield the same RMS difference. Every station on the shelf has two or more stations that can be differenced with to achieve RMS ≤ 2 cm—down from the 3.7–6.9 cm noted above—with the exception of LT20 and LT11, which have no such pairs. Likewise, all stations on the continental slope have two or more stations that they can be differenced with to achieve RMS ≤ 1 cm—down from the 2.2–2.9 cm noted above—except LA22, which has none. Given the broad geographic footprint and relative sparsity of the AACSE network, it is difficult to discern precise limits on depth difference and range between station pairs to yield a given RMS threshold. However, some tentative correlation scales can be gleaned from the station pair differences. On the shelf, to yield signal RMS ≤ 2 cm over separations as large as 422 km, there may be two distinct regimes; for stations at depths ≥ 156 m depth differences can be as large as 120 m and for those at ≤ 125 m depths differences must be ≤ 42 m. On the slope, to achieve RMS ≤ 1 cm differences over separations as large as 470 km there may be a deeper regime (depths $\geq 2,622$ m) where depth differences can be as large as 1,990 m, and a shallower regime (depths $\leq 2,130$ m) where depth differences are limited to 1,058 m. These limits are dependent on the spatially sparse data available from the AACSE. It should also be noted that there are station pairs within these bounds that do not result in the RMS thresholds given, suggesting more complexity in the constraints on depth-matched pressure coherence.

4.2. Proxy Efficacy for Correcting for Oceanographic Pressure Signals

We consider RMS reduction as a measure of the extent to which a given seasonal correction and/or proxy can remove oceanographic signals, again noting that this measure may not strictly correspond to increased detectability of SSE-like signals. RMS reduction is defined as:

$$\text{RMS reduction} = 1 - \frac{\text{RMS (corrected data)}}{\text{RMS (uncorrected data)}}$$

The RMS reduction depends on the site and all forms of corrections considered herein, so we provide only a summary here and present full data in Figure 6 (sinusoidal and pressure-CEO² corrections), Figure S4 in Supporting Information S1 (polynomial and m-CEO² corrections), and Tables S3 and S4 in Supporting Information S1. For the shelf sites, the sinusoidal correction alone (Figure 6a and Table S3 in Supporting Information S1) yields RMS reductions of 6%–24%. The net RMS reductions achieved with subsequent proxy applications are similar for P_{match} and P_{avg} at 53%–80%, for P_{SSH} they generally increase with decreasing station depth and range from 12% to 54%, and P_{temp} makes negligible improvement. Application of the pressure-CEO² correction alone on the shelf (Figure 6c and Table S4 in Supporting Information S1) reduces the RMS by 54%–73%, and further application of P_{match} or P_{avg} raises the upper limit of net RMS reduction to 83% and 80%, respectively. Interestingly, though P_{ref} generally does not further reduce RMS, the two shallowest stations (LT10 and LT12) prove an exception.

For the slope sites, the sinusoidal correction (Figure 6b and Table S3 in Supporting Information S1) yields RMS reductions from 2% to 17%, and again P_{match} and P_{avg} perform comparably with a net reduction to 54%–86%. The net RMS achieved with P_{ref} roughly scales with station depth, from 13% at one of the shallower sites to 41% for the deepest site. Pressure-CEO² corrected slope pressures (Figure 6d and Table S4 in Supporting Information S1) have RMS reductions of 53%–80%. P_{match} and P_{avg} are the only proxies to provide a notable further RMS reduction, but only for a few sites where they achieve maximum reductions of 83% and 93%, respectively.

Figure S4 in Supporting Information S1 summarizes proxy RMS reduction for polynomial and multivariate-CEO² corrected data. The polynomial results are highly comparable to the sinusoidal results, while the multivariate-CEO² results fall somewhere between those of the pressure-CEO² and the functional corrections. Across all locations and seasonal corrections, the proxies P_{match} and P_{avg} tend to yield the greatest RMS reductions.

Figure 5. Plots of difference root-mean-square error (RMS) for all station combinations as a function of separation and depth difference, after tidal filtering, drift correction, and sinusoidal seasonal correction. Symbol shapes correspond to individual stations and colors scale with RMS. Negative depth differences mean that the station indicated by the marker is shallower than the station that has been subtracted from it. (a) All shelf pairs (depths 83–262 m). (b) Shelf pairs at depths 83–125 m. (c) Shelf pairs at depths 156–262 m. We highlight station pairs that include LT11 and/or LT20, which may be anomalous (see text), by outlining them in bold black. (d) All slope pairs (depths 1,564–4,612 m). (e) Slope pairs at depths 1,564–2,130 m. (f) Slope pairs at depths 2,622–4,612 m. Vertical dashed lines in (d)–(e) mark the depth range limits considered in (a), highlighting the difference in scale. As the only station beyond the trench, LA21 is excluded from these comparisons.

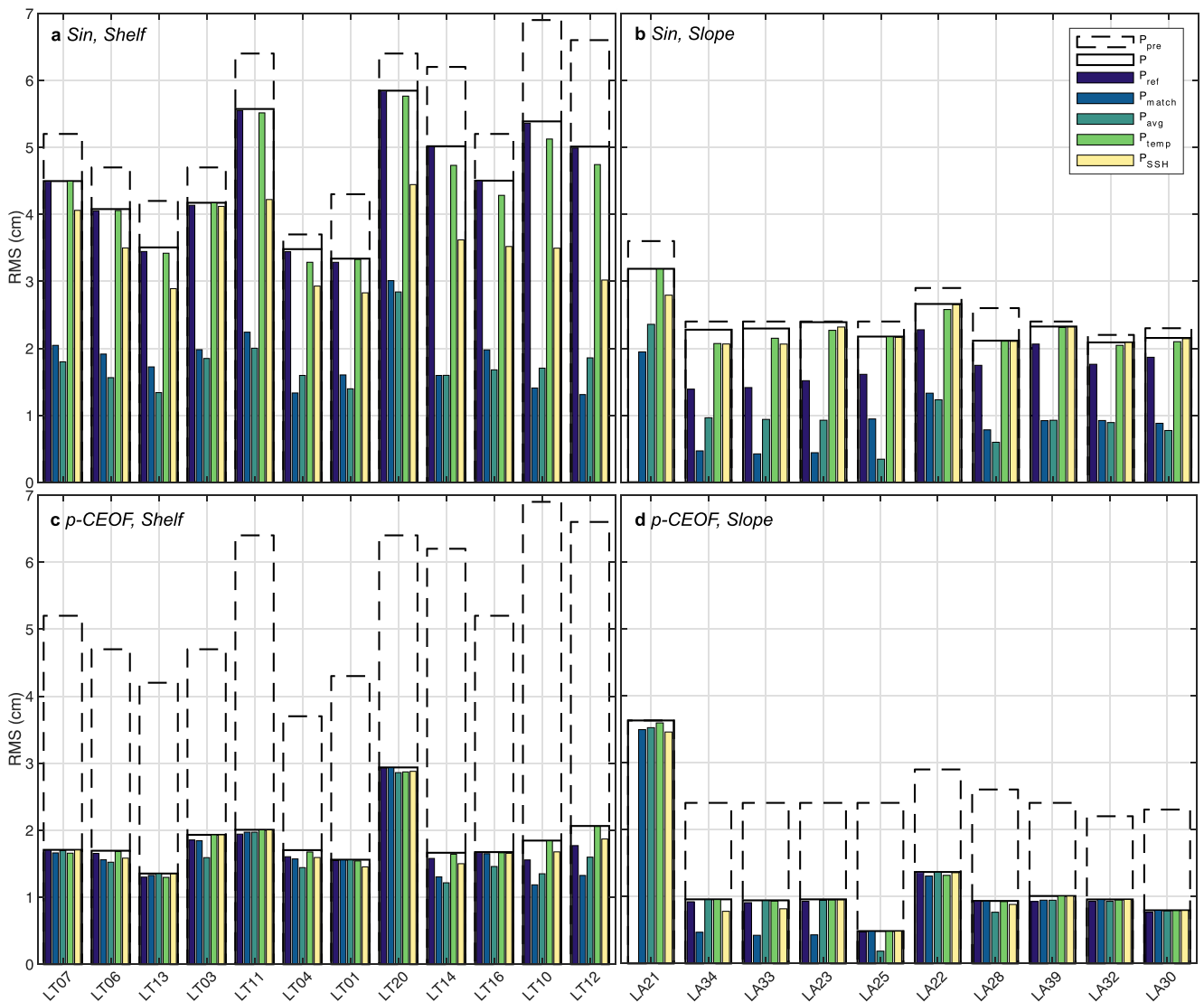


Figure 6. Proxy-corrected pressure root-mean-square error (RMS) improvements for sinusoidally corrected (a) shelf and (b) slope data, and pressure-complex empirical orthogonal function (p-CEOFL) corrected (c) shelf, and (d) slope data. The empty, black-outlined bars in the background show the RMS of the seasonally corrected pressure record before applying any proxy, while the thin colored bars show the RMS of each proxy corrected time series.

4.3. Identification and Characterization of SSE Transients

4.3.1. Known Onset Time

The seasonal and proxy corrections considered herein yield a large number of combinations from which to assess detectability. For simplicity, we focus on the sinusoidal and pressure-CEOFL methods, noting that the sinusoidal and polynomial results are comparable and the pressure-CEOFL results yield better overall detectability than the multivariate-CEOFL results. A summary of the full results is provided in Table 1.

Figure 7 shows the amplitude recovery error from our detectability analysis for shelf stations when onset timing is assumed known, as might be the case if constrained by coastal GNSS data or other observables (e.g., Wallace et al., 2016). With known onset timing, our detector does not depend on the synthetic SSE amplitude because it is masked out (see Section 3.4). With the exceptions of multivariate-CEOFL + P_{ref} on the shelf and pressure-CEOFL + P_{avg} on the slope, all processing and proxy methods yield amplitude recovery results with medians within 1 cm of the known value, but with significant differences in distribution around the median (Figure 7, Figures S5 and S6 in Supporting Information S1). To meaningfully compare correction techniques, we present results in terms of median plus or minus the median absolute deviation (MAD).

Table 1

Summary of Synthetic Detectability Results When Onset Is Assumed Known

Proxy		Amplitude recovery error (cm)			
		Shelf		Slope	
		Median	Mad	Median	Mad
POLY	P	0.8	5.4	-0.4	1.4
	Pref	0.8	5.4	-0.4	1.4
	Pmatch	-0.5	1.6	-0.2	0.6
	Pavg	-0.5	1.7	-0.2	1.1
	Ptemp	0.2	4.9	-0.5	1.1
	Pssh	-0.7	2.7	-0.7	1.1
SIN	P	0.9	5.4	-0.3	1.6
	Pref	0.7	5.6	-0.3	1.7
	Pmatch	-0.5	1.5	-0.2	0.6
	Pavg	-0.4	1.7	-0.1	1.5
	Ptemp	-0.1	4.4	-0.6	1.1
	Pssh	-0.2	3.3	-0.6	1.1
m-CEO	P	-1.8	3.1	-0.6	1.0
	Pref	-2.1	2.0	-1.2	1.2
	Pmatch	-1.8	1.3	-1.2	1.0
	Pavg	-1.9	1.4	-1.2	1.1
	Ptemp	-2.3	2.4	-1.3	1.2
	Pssh	-2.2	2.4	-1.4	1.2
p-CEO	P	-0.1	1.3	-0.1	1.0
	Pref	-0.1	1.3	-0.6	1.0
	Pmatch	-0.2	1.0	-0.5	0.6
	Pavg	-0.1	2.3	-1.9	1.8
	Ptemp	-0.2	1.2	-0.2	0.9
	Pssh	-0.3	1.2	-0.4	0.9

Note. Amplitude recovery error for the known onset case is summarized as median and MAD values for the combined predictions from all ramp amplitudes considered herein, for all combinations of seasonal and proxy corrections considered in this study, with shelf and slope presented separately. The values for each seasonal/proxy pair result from 552 synthetic detection results on the shelf and 414 results on the slope. Light gray cells indicate median \pm MAD ranges that fall within -1.5 to +1.5 cm of the known value. Dark gray cells indicate a range of -1.0 to +1.0 cm m-CEO, multivariate-CEO; p-CEO, pressure-CEO.

On the shelf, the pressure-CEO yields significantly tighter distributions than the other three seasonal correction methods, and notably the application of proxy corrections results in negligible improvement relative to the no-proxy cases and regardless of the varying RMS reductions associated with each proxy (Figure 7, Figure S6 in Supporting Information S1, Table 1). The tightest distributions, for the pressure-CEO case, have median \pm MAD ranges within -1.5 to 1.5 cm of the known value for the no-proxy, P_{ref} , P_{match} , P_{temp} , and P_{SSH} (light gray shading in Table 1). P_{avg} is the only exception here, with an anomalously large median \pm MAD range of -2.8 to 2.2 cm, while the multivariate-CEO method with P_{avg} yields the smallest range of -1.6 to 0.8 cm (Table 1). Across polynomial, sinusoidal, and multivariate-CEO seasonal corrections, the tightest distributions result from P_{match} and P_{avg} , with median \pm MAD ranges of -2.2 to 1.7 cm or better.

On the slope (Figures S5 and S6 in Supporting Information S1), the differences in results between methods are similar but more subtle, with all yielding MADs \leq 1.8 cm. Here also, the pressure-CEO seasonal correction consistently yields the most favorable median \pm MAD ranges, -1.5 to 1.5 cm or better for no proxy, P_{match} , P_{temp} , and P_{SSH} (Table 1). Unlike the shelf, the application of the P_{match} proxy consistently reduces the MAD relative to using none. Poor performance is again seen for pressure-CEO with P_{avg} , yielding a range of 0.0–3.6 cm. Comparing all methods, polynomial, sinusoidal, and multivariate-CEO seasonal corrections with P_{match} , as well as pressure-CEO with no proxy, yield the best ranges, at -1.0 to 1.0 cm or better (dark gray shading in Table 1).

4.3.2. Unknown Onset Time

For unknown onset timing, we consider each proxy's efficacy in predicting the ramp onset time (Figures 8a–8f) as well as its amplitude (Figures 8g–8l). Though our detector still assumes the presence of a ramp, in the absence of known timing the ramp amplitude does affect the detectability. For simplicity, in Figure 8, we display only two detectability distributions on the shelf: the sinusoidal and pressure-CEO seasonal corrections with P_{match} . These two correction methods were chosen because of both their high degree of RMS reduction (Tables S3 and S4 in Supporting Information S1) and for the accuracy of their known-time detection distributions (Figure 7c, Figure S5c in Supporting Information S1, Table 1). Summary results for all seasonal corrections and for the proxies P_{match} , P_{avg} , and no proxy are detailed in Table 2.

As with the detectability distributions in the known timing case, we assess ramp detectability under the various scenarios by the median \pm MAD. We first summarize results on the shelf and for the pressure-CEO seasonal correction. For a 4-cm ramp, pressure-CEO with P_{match} is the only method that can meaningfully localize the onset, yielding estimated median \pm MAD

ranges of -6 to 8 days and of 2.1–5.1 cm (Figures 8c and 8i and Table 2). A 3.5-cm ramp was also tested, but its onset could not be constrained by any method (Table S5 in Supporting Information S1). For 6-cm ramps, several processing combinations yield distributions that are well localized in time, the best among these being pressure-CEO with either no proxy or P_{match} providing median \pm MAD ranges of -3 to 3 days (Figure 8d) and 4.3–7.1 cm or better (Figure 8j). Notably, using the P_{match} proxy provides negligible improvement relative to the no-proxy case. For 8-cm and 10-cm ramps, predicted onset distributions become increasingly comparable between seasonal and proxy correction methods—as good as -2 to 2 days with amplitude MADs of 1.2 cm—with the exceptions of no-proxy polynomial and sinusoidal seasonal corrections performing significantly worse. This reflects both the tendency for functional seasonal corrections to incorporate some of the ramp signal and the simplification of treating the CEOF corrections as purely seasonal. Detection results for the polynomial

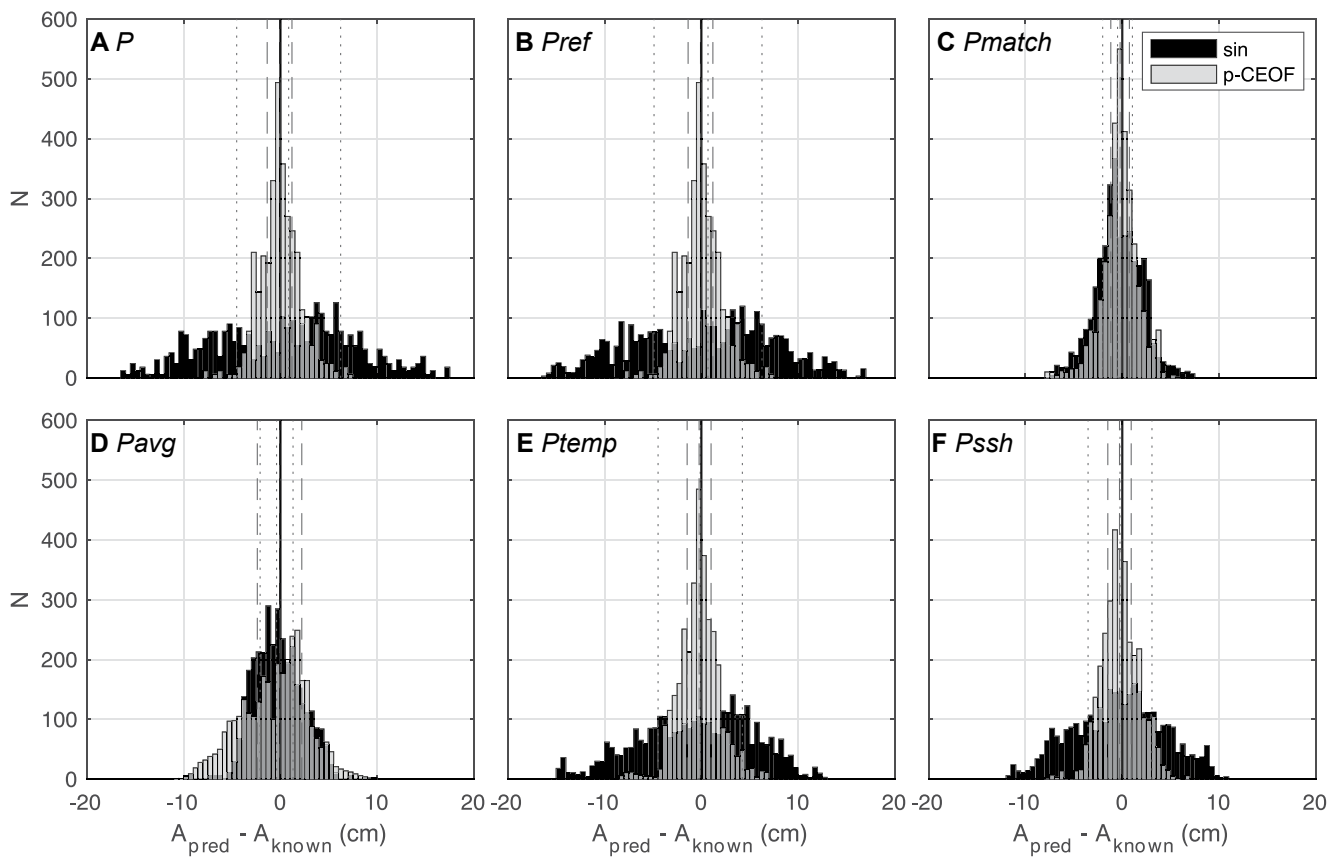


Figure 7. Histograms showing amplitude recovery error from the synthetic slow slip event detection analysis on the continental shelf, when known onset time is assumed, using sinusoidal (black), and pressure-complex empirical orthogonal function (p-CEOFO, translucent gray) seasonal corrections, for each of the proxies considered. The results from all synthetic ramp amplitudes considered (0, 2, 4, 6, 8, and 10 cm) were combined, with ramp duration held at 14 days and onset times varied weekly from August 2018 through April 2019. (a) No proxy. (b) P_{ref} (c) P_{match} . (d) P_{avg} . (e) P_{temp} . (f) P_{SSH} . Vertical solid lines indicate the desired result ($A_{\text{pred}} - A_{\text{known}} = 0$), vertical dotted lines show the median and \pm MAD of the error for the sinusoidal case, and vertical dashed lines show the same for the pressure-CEOFO case.

and multivariate-CEOFO seasonal corrections are shown in Figure S8 in Supporting Information S1. Across all processing techniques and input amplitudes, when the onset time is estimated accurately, the detector tends to underpredict ramp amplitude.

For the slope, a summary of the full detectability analysis for unknown onset timing is given in Table 2, while Figure S7 in Supporting Information S1 plots the detection distributions for the sinusoidal and pressure-CEOFO seasonal corrections with P_{match} proxy applied. In this setting, a 2-cm ramp can only be meaningfully constrained by either of the pressure-CEOFO or multivariate-CEOFO seasonal corrections, in conjunction with P_{match} , yielding median \pm MAD range of -7 to 7 days or better and -1.0 to 2.6 cm or better (Figures S7b and S7h in Supporting Information S1 and Table 2). A 1.5-cm ramp was also tested, but its onset could not be constrained by any method (Table S5 in Supporting Information S1). For amplitudes 4 cm and above, timing accuracy improves rapidly and equalizes across seasonal and proxy corrections. At 4 cm, all seasonal corrections with P_{match} have median \pm MAD ranges of -2.0 to 2.0 days and 2.7 – 4.3 cm or better. By 6 cm, all methods except polynomial and sinusoidal with no proxy and pressure-CEOFO with P_{avg} yield median \pm MAD ranges of -3 to 3 days and 3.8 – 7.2 cm or better. Detection results for the polynomial and multivariate-CEOFO seasonal corrections are shown in Figure S9 in Supporting Information S1. Even when the timing is estimated well, the amplitude tends to be underpredicted, though to a lesser degree than is seen on the shelf.

Tests for the null case (i.e., a 0-cm synthetic ramp) provide some insight on false detections (Figure 8g). In the absence of a ramp on the shelf, the pressure-CEOFO seasonal correction with P_{match} yields the tightest distributions, with a median \pm MAD of 1.9 ± 1.7 cm. On the slope, the pressure-CEOFO seasonal correction and P_{avg} yield the tightest distributions, with a median \pm MAD of 0.0 ± 0.5 cm, but we deem this to be anomalous and instead infer

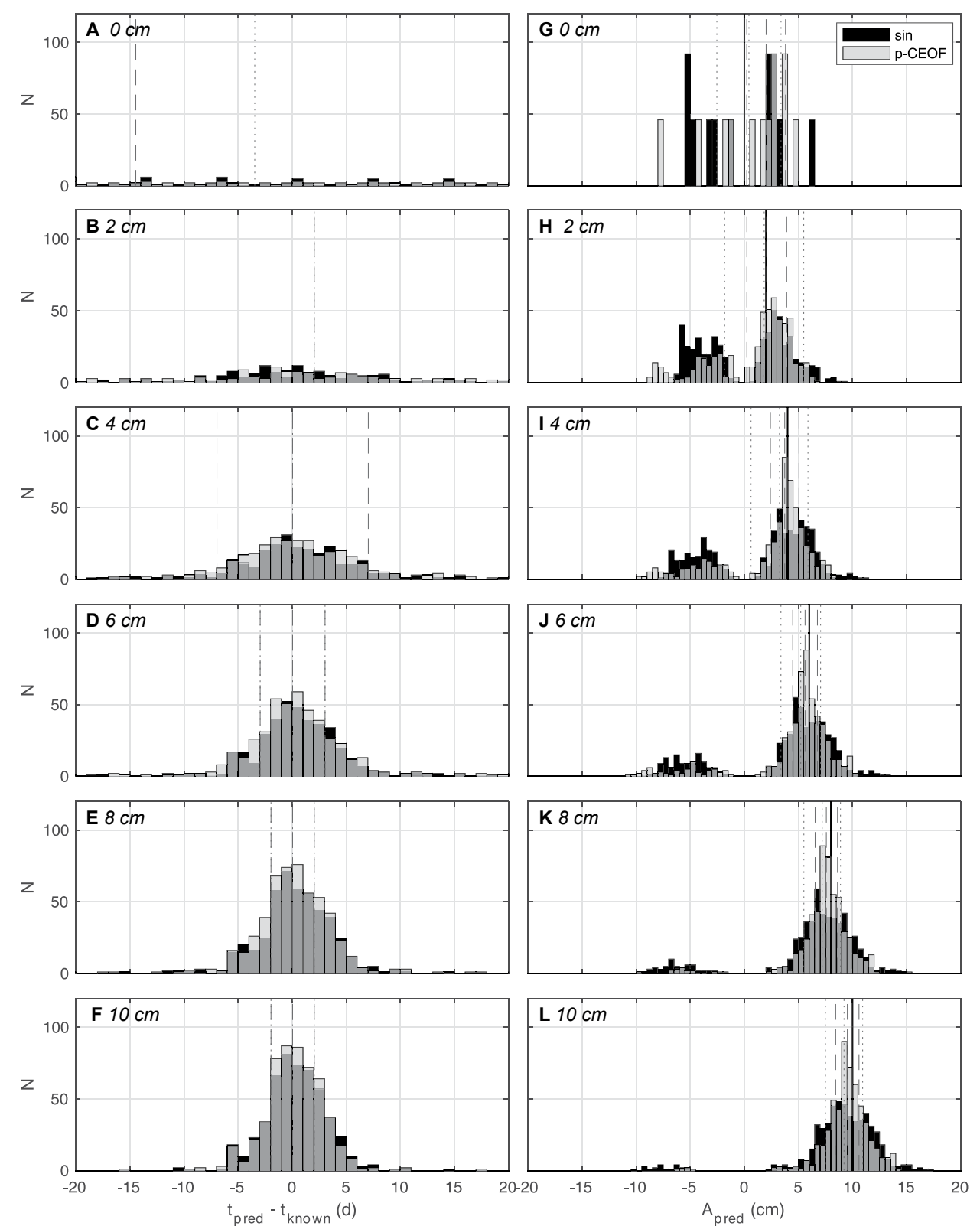


Figure 8.

$\sim 1 \pm 1$ cm to be more probable, given the values seen across other processing methods. False detections appear significantly more probable with the functional form seasonal corrections and no proxy, yielding shelf and slope median \pm MADs of $\sim -12 \pm 2$ and $\sim 4 \pm 1$ cm, respectively.

For both shelf and slope locations, the worst onset time predictions are seen to arise from the detector misidentifying signals unrelated to the synthetic ramps (Figure S12 in Supporting Information S1). On the shelf, most of these poor detections arise in September–October, mid-January to early February, at the end of the time series, and predominantly from a subset of stations. On the slope, the worst predictions are more broadly dispersed in time, but again principally occurring at only a subset of stations.

The detectability results described above hold for ramps as short as 1 day (Figure S10 in Supporting Information S1, shelf; Figure S11 in Supporting Information S1, slope). When attempting to detect longer ramps, the distributions broaden, to a greater extent in time than in amplitude, and amplitude distributions also shift toward greater underprediction (Figures S10 and S11 in Supporting Information S1).

5. Discussion

5.1. RMS as a Metric for SSE Detectability

Our results permit us to assess the applicability of pressure record RMS as a predictor of the accuracy of SSE detection and characterization. RMS reduction is commonly used in pressure geodesy as a measure of a proxy's ability to reduce oceanographic signals, but its sensitivity to oscillatory signals in addition to ramp-like SSE signals suggests it may not represent a proxy's potential to improve SSE detection and characterization, as is generally assumed. Indeed, a significant component of pressure signals, particularly on the shelf, result from highly oscillatory weather-band energy (Luther et al., 1990), as has been observed in seafloor pressures offshore New Zealand and Japan (Gomberg et al., 2019; Johnson et al., 2017). Further, signal RMS changes with time, becoming notably elevated in the winter months. Our results suggest that RMS is only a first-order measure of SSE detectability and that RMS differences of a few millimeters are not predictive. For example, when assuming known onset timing, the corrections that yield the greatest RMS reduction (Tables S3 and S4 in Supporting Information S1) likewise tend to yield the best-constrained amplitude predictions (gray shading in Table 1), but the differences between these predictions are small and do not correlate with RMS reduction. Notably, pressure-CEOFS with P_{match} yields better RMS reductions on the slope than pressure-CEOFS with no proxy and yet the latter ostensibly outperforms the former in its amplitude predictions. When onset timing is unknown, the corrections that yield the greatest RMS reduction (Tables S3 and S4 in Supporting Information S1) yield the best timing predictions for ramps just above the threshold of predictability, but these timing predictions and the resultant amplitude predictions equalize across processing methods as larger ramps are considered (gray shading in Table 2).

5.2. Implications of Observed Seafloor Pressure Spatial Coherence

The efficacy of the CEOF-based seasonal corrections and the proxies P_{match} and P_{avg} for removing non-tidal oceanographic signals (Figure 6, Tables S2 and S3 in Supporting Information S1) is a consequence of the remarkable coherence of the bottom pressure anomaly field over the ~ 970 km span of the AACSE network. Such broad spatial scales are characteristic of water column processes (e.g., Hughes & Meredith, 2006). While this signal similarity holds across the shelf and slope regimes, it is strongest within broad, coherent bathymetric features such as the Shelikof Trough (Figure 1). In addition, the breakdown of this coherence in the case of LT20 (the only shelf station west of the Shumagin Islands) and LA21 (the only deep station outboard of the lower slope Alaska Boundary Current) suggests that distinct coherent oceanographic domains exist beyond the simple shelf/slope demarcation described here.

The seafloor pressure coherence seen in Alaska can be compared to similar studies in Cascadia (Fredrickson et al., 2019) and Hikurangi (Inoue et al., 2021), bearing in mind the observational sparsity in all three settings. It

Figure 8. Histograms displaying slow slip event onset errors and amplitude predictions as a function of input ramp amplitude from synthetic detection analysis on the shelf, for unknown onset times, for sinusoidal (black) and pressure-complex empirical orthogonal function (p-CEOFS, translucent gray) seasonal corrections, using only our best-performing proxy, P_{match} . Synthetic ramp duration was held constant at 14 days and onset times were varied weekly from August 2018 through April 2019 to generate the composite distributions shown. (a–f) Timing recovery for synthetic ramps of 0, 2, 4, 6, 8, and 10 cm amplitude. Vertical dotted lines show the median and \pm MAD for the sinusoidal case, while vertical dashed lines show the same for the pressure-CEOFS case. (g–l) Amplitude recovery for synthetic ramps of 0, 2, 4, 6, 8, and 10 cm amplitude. Vertical solid lines show the input synthetic amplitude, vertical dotted lines show the median and \pm MAD for the sinusoidal case, and vertical dashed lines show the same for the pressure-CEOFS case.

Table 2
Summary of Synthetic Detectability Results When Onset Is Assumed Unknown

Aknown (cm)	Proxy	Shelf						Slope			
		Onset recovery error (d)		Amplitude recovery (cm)		Onset recovery error (d)		Amplitude recovery (cm)			
		Median	Mad	Median	Mad	Median	Mad	Median	Mad	Median	Mad
0	POLY	P	36.0	84.0	-12.4	2.4	43.5	80.5	1.9	1.1	
		Pmatch	-15.0	84.0	0.4	2.7	7.0	82.5	0.5	2.3	
		Payg	-24.5	84.0	0.3	3.6	24.0	83.0	3.0	0.8	
	SIN	P	50.0	80.5	-12.0	2.0	31.0	83.0	3.3	1.5	
		Pmatch	-3.5	94.5	0.4	3.0	37.5	82.5	-0.8	2.4	
		Payg	4.0	84.0	3.9	1.5	-4.5	85.5	3.7	0.9	
	m-CEO	P	33.0	94.0	4.4	1.4	-25.5	96.5	-0.5	1.3	
		Pmatch	-26.5	93.5	-1.4	1.0	55.0	81.5	0.5	0.9	
		Payg	-16.5	93.0	-1.1	1.1	42.0	80.5	1.7	0.5	
	p-CEO	P	-13.0	88.5	2.8	2.3	-25.5	96.5	-0.7	1.4	
		Pmatch	-14.5	88.5	2.0	1.8	69.0	84.0	1.5	1.3	
		Payg	-2.0	84.5	3.7	3.2	18.0	98.0	0.8	0.6	
2	POLY	P	36.0	84.0	-12.5	2.3	14.0	58.0	2.7	1.1	
		Pmatch	-2.0	78.0	-1.5	3.6	0.0	34.0	1.8	1.3	
		Payg	-5.5	72.5	2.9	2.1	2.0	61.0	2.9	1.1	
	SIN	P	43.0	84.0	-11.3	2.5	8.0	58.0	2.8	1.3	
		Pmatch	2.0	74.5	1.8	3.7	0.0	25.5	1.8	1.9	
		Payg	-2.0	79.0	3.4	2.2	-1.0	52.0	3.1	1.7	
	m-CEO	P	37.5	89.5	4.3	1.5	-7.0	77.5	0.4	1.8	
		Pmatch	1.5	65.5	-0.7	2.3	0.0	7.0	1.5	0.8	
		Payg	2.0	60.5	-0.2	1.9	5.0	63.5	1.5	1.2	
	p-CEO	P	1.5	79.0	3.0	2.1	-7.0	77.5	0.6	2.3	
		Pmatch	2.0	75.0	2.1	1.8	-1.0	7.0	2.0	0.5	
		Payg	2.0	84.0	1.3	3.7	-3.0	84.5	0.0	2.2	
4	POLY	P	30.0	84.0	-12.6	2.5	2.0	30.5	3.4	1.5	
		Pmatch	-1.0	29.0	2.7	3.7	0.0	3.0	3.7	0.7	
		Payg	-1.0	58.0	3.4	2.5	0.0	9.0	3.6	1.4	
	SIN	P	36.0	84.0	-11.6	2.9	1.5	18.5	3.6	1.7	
		Pmatch	0.0	23.5	3.2	2.6	0.0	3.0	3.8	0.8	
		Payg	-1.0	51.0	3.8	2.7	0.0	6.5	4.1	1.9	
	m-CEO	P	13.5	77.5	4.3	2.4	0.0	20.0	2.0	2.7	
		Pmatch	3.0	46.0	1.8	2.4	0.0	3.0	2.7	0.9	
		Payg	3.0	51.5	1.3	2.5	3.0	10.0	2.6	1.2	
	p-CEO	P	0.0	12.0	4.0	1.6	0.0	20.0	2.8	2.8	
		Pmatch	0.0	7.0	3.7	1.3	0.0	2.0	3.6	0.7	
		Payg	0.0	12.0	2.7	3.5	1.0	20.0	0.5	2.9	
6	POLY	P	23.0	83.0	-12.8	3.0	0.0	8.0	4.8	1.9	
		Pmatch	0.0	4.0	4.7	2.4	0.0	2.0	5.7	0.7	
		Payg	0.0	7.0	4.6	2.2	0.0	2.0	5.5	1.2	
	SIN	P	29.5	80.5	-11.6	3.8	0.0	5.0	5.4	2.0	

Table 2
Continued

Aknown (cm)	Proxy	Shelf				Slope					
		Onset recovery error (d)		Amplitude recovery (cm)		Onset recovery error (d)		Amplitude recovery (cm)			
		Median	Mad	Median	Mad	Median	Mad	Median	Mad		
8	POLY	Pmatch	0.0	3.0	5.2	1.8	0.0	1.0	5.8	0.6	
		Pavg	0.0	6.0	5.1	2.4	0.0	2.0	6.0	1.6	
		m-CEO	P	4.0	59.0	4.6	2.7	0.0	3.0	4.8	1.4
		Pmatch	2.0	12.0	3.1	1.9	0.0	2.0	4.3	0.9	
		Pavg	2.0	33.0	2.6	2.0	1.0	5.0	4.2	1.1	
		p-CEO	P	0.0	4.0	5.8	1.4	0.0	3.0	5.5	1.4
10	POLY	Pmatch	0.0	3.0	5.6	1.1	0.0	1.0	5.5	0.6	
		Pavg	0.0	4.0	4.7	3.0	0.0	3.0	3.1	2.1	
		SIN	P	22.5	66.5	-10.6	6.0	0.0	3.0	7.3	1.8
		Pmatch	0.0	2.0	7.0	1.9	0.0	1.0	7.7	0.6	
		Pavg	0.0	3.0	6.5	2.1	0.0	1.0	7.6	1.3	
		m-CEO	P	2.0	25.5	5.5	2.8	0.0	2.0	6.9	1.1
12	POLY	Pmatch	1.0	4.0	4.4	1.7	0.0	1.0	5.8	1.0	
		Pavg	1.0	5.0	4.0	1.6	0.0	4.0	5.9	1.0	
		p-CEO	P	0.0	2.0	7.9	1.3	0.0	2.0	7.9	1.0
		Pmatch	0.0	2.0	7.6	1.0	0.0	1.0	7.3	0.7	
		Pavg	0.0	3.0	7.4	2.3	0.0	2.0	5.1	1.9	
		SIN	P	16.0	71.0	-12.3	4.7	0.0	3.0	9.3	1.7
14	POLY	Pmatch	0.0	2.0	9.0	1.8	0.0	1.0	9.7	0.6	
		Pavg	0.0	2.0	8.5	2.0	0.0	1.0	9.6	1.2	
		SIN	P	17.5	53.5	-7.3	12.1	0.0	2.0	9.4	1.7
		Pmatch	0.0	2.0	9.2	1.7	0.0	1.0	9.7	0.6	
		Pavg	0.0	2.0	9.0	1.9	0.0	1.0	9.9	1.5	
		m-CEO	P	0.0	5.5	6.3	2.9	0.0	1.5	8.8	1.1
16	POLY	Pmatch	0.0	3.0	5.8	1.5	0.0	1.0	7.4	1.0	
		Pavg	0.0	3.0	5.3	1.4	0.0	3.0	7.5	1.1	
		p-CEO	P	0.0	2.0	9.9	1.3	0.0	1.5	9.9	1.0
		Pmatch	0.0	2.0	9.5	1.1	0.0	1.0	9.1	0.7	
		Pavg	0.0	2.0	9.4	2.1	0.0	2.0	6.6	2.1	

Note. Onset recovery error and amplitude recovery for the unknown onset case are summarized as median and MAD errors for each ramp amplitude considered herein for all seasonal corrections, and the proxy corrections P , P_{match} , and P_{avg} , with shelf and slope presented separately. Light gray cells indicate onset prediction median \pm MAD ranges that fall within -8 to +8 days of the known value. Dark gray cells indicate ranges that fall within -4 to +4 days of the known value. m-CEO, multivariate-CEO; p-CEO, pressure-CEO.

should first be noted that, on a broad scale, pressure data have larger amplitudes in Alaska than in either Cascadia or Hikurangi and as a result, even the most effective seasonal and proxy corrections yield larger RMS values. At shelf sites in Alaska (83–262 m depth), RMS \leq 2 cm and as low as 1.3 cm can be—but is not always—achieved between sites with depth differences \lesssim 100 m with no consistent improvement when the depth difference is

reduced to $\lesssim 50$ m. In contrast, on the Cascadia shelf for 120–177 m depth, RMS of ≤ 1.7 cm and as low as 0.7 cm can be obtained from sites with depth differences $\lesssim 50$ m, with some exceptions. Analysis of Hikurangi shelf pressure records is not available in the literature. Thus, to first order, the available data suggest that the proxy P_{match} can be more flexibly defined on the shelf in Alaska but proves to be a more effective correction on the shelf in Cascadia.

At slope sites in Alaska, RMS values of ≤ 1 cm may be achieved for station pairs at 1,564–2,130 m depth over the full ~ 500 m depth difference range, with some exceptions, and RMS values of ≤ 1 cm may be achieved for sites at 2,622–4,612 m depth for depth differences of $\sim 2,000$ m. In Cascadia, differences between upper slope sites (675–1,297 m) yield RMS values ≤ 1 cm for depth differences $\lesssim 400$ m, and all differences for sites at depths 1,400–2,908 m yield RMS values ≤ 0.9 cm with many ≤ 0.5 cm (Fredrickson et al., 2019). For upper slope sites in Hikurangi (651–1,031 m depth), RMS values ≤ 1 cm are seen when depth differences are $\lesssim 350$ m, while for lower slope and abyss sites (1,246–3,538 m depth), RMS values ≤ 1 cm (many ≤ 0.5 cm) are seen for depth differences up to $\sim 2,000$ m (Inoue et al., 2021). Thus, given the limited extent of the networks in each location, the appropriate depth difference and separation scales for shallow slope sites are approximately the same across localities to minimize difference RMS to ≤ 1 cm. On the lower slope, these scales are likewise comparable between localities, but with evidence for Cascadia and Hikurangi having a lower noise floor than is seen in Alaska. We also note that in the Nankai Trough, RMS values averaging 1.1 cm were obtained for DONET pressures at $\sim 1,500$ –4,500 m depth (e.g., Kawaguchi et al., 2015) recorded on sensors grouped in sub-networks of five instruments spaced ~ 20 km apart, after subtracting the mean pressure record for the respective subnet (Suzuki et al., 2018). It is notable that only in Alaska do we see a distinct incoherence between abyssal plain and lower slope sites, regardless of depth difference or separation. In Alaska and Cascadia, all of the above relationships hold true over site separations of hundreds of kilometers and in Hikurangi over separations of at least 80 km (the diameter of the network). Overall, these comparisons suggest that across multiple margins, the circulation processes that contribute significantly to seafloor pressures are temporally and spatially uniform along isobaths, within the hourly sampling considered here and subject to some linear scaling factor between sites.

The proxies based on other water column properties (seafloor temperature and SSH) at sites collocated with the pressures, seafloor temperature, and SSH herein, do not appear to serve as effective proxies when used in the analyses employed here. However, their use warrants further investigation because they do not rely on multiple recording sites nor assumptions about spatial coherence, and they may provide qualitative indicators of oceanographic signals that could be misconstrued as tectonic in origin. For example, on the shelf, P_{SSH} yields only modest reductions in signal RMS (Figure 6 and Table S3 in Supporting Information S1), likely because of the difference in frequency content when compared with the more continuously sampled seafloor records. However, it nonetheless tracks the abrupt seasonal transitions in October and February (Figures 3a and 3f). This observation is consistent with model simulations and published information on climatic and oceanographic patterns in the region, which show that during the winter months, strong winds transport water onto the shelf and cause downwelling of warmer water, creating winter-time peaked elevated sea levels, seafloor warming, and pressure increases (Stabeno et al., 2004). Any potential deformation that occurs during the transitions between summer and winter is prone to conflation with that seasonal shift, making it difficult to isolate empirically. We observe that these seasonal shifts differ enough between locations to not be reliably corrected during differencing (Figures 3c and 3d). Thus, if not carefully accounted for, climatically driven seasonal variations in P_o and proxy data may mask or lead to a misleading amplitude prediction for P_G , particularly when only a single or incomplete seasonal cycle is recorded (Gomberg et al., 2019). A benefit of SSH data is the fact that they are routinely collected and readily available globally. Further, the spatial resolution of SSH grid requires interpolation to station locations, but nonetheless yields promising results. Future increases in spatial and temporal resolution of these satellite products may prove to be increasingly effective predictors of seafloor pressure.

There is very little RMS reduction provided by P_T (Figure 7), consistent with prior studies by Baba et al. (2006), Gomberg et al. (2019), and Itoh et al. (2019). However, qualitatively inspecting and comparing the time series reveals that there are certain frequencies and time periods at which the two signals correlate well, particularly on the shelf. This indicates that, as one might expect, there is a physical relationship between bottom temperature and pressure, but that it is temporally and spatially variable. As with SSH, this relationship has the potential to provide an additional means of differentiating tectonic and oceanographic signals and warrants further study. Additional independent measurements warrant exploration as P_o proxies, but require a deeper understanding of ocean circulation processes that may be region-specific.

5.3. Maximizing SSE Detectability in Pressure Records

We summarize some of the limitations associated with the detectability analysis presented herein. First, we have assumed that there is only one SSE signal present on a single station in the network at any time, which is reasonably consistent with the AACSE network geometry and the anticipated spatial scale of SSE deformation based on other studies. However, the higher site density in the western end of the AACSE or in other networks does not preclude the possibility of recording SSE deformation at multiple sites, as reported by He et al. (2021). Second, the methods that assume spatially coherent oceanographic pressures at multiple sites may inadvertently correct out some component of P_G , particularly those using the CEOF seasonal corrections and proxy P_{avg} and P_{match} for poorly chosen site pairs. We minimized this possibility by masking out deformation signals before calculating the CEOFs and by excluding the station containing the synthetic deformation signal from the calculation of P_{avg} , but in a real scenario, this would not be as straightforward. In smaller aperture networks or those with larger instrument density (e.g., Woods et al., 2022), these concerns are amplified as it may be difficult or impossible to exclude proximal stations. However, in such settings, the pressure-CEOFO seasonal correction and P_{avg} proxy have the benefit of being sensitive to sign and so in a well-recorded SSE the records of uplift and subsidence would tend to cancel one another out in their P_G terms. Further, in the case of known onset time or even known approximate location SSEs, efforts could be made to exclude particular stations from calculations or to mask the P_G period of the signal. We also caution that with all of the seasonal corrections considered here there is risk of correcting out or aliasing some part of P_G , so none should be used blindly. Finally, the detector is designed to perform optimally when the SSE ramp is the only significant signal present, which as noted in Section 4.3.2 is not always the case even with our best-corrected pressure data.

Our detectability results show that there is a significant benefit to having independent information about the onset time (e.g., coastal GNSS deformation signals), particularly for smaller SSEs. In the end-member case of a 0-cm (null) SSE ramp, knowing the event onset a priori yields a median \pm MAD range as good as -1.3 to 0.9 cm on the shelf (pressure-CEOFO and P_{match} , Table 1), as compared to 0.2 – 3.6 cm when event timing is unknown (pressure-CEOFO and P_{match} , Table 2). For larger ramps, onset constraint improves for the unknown timing case and consequently amplitude predictions more closely compare to those from the known timing case, though general amplitude underprediction remains. This underprediction results in part from the bimodal distributions of the recovered amplitudes when timing is unknown (Figure 8 for the shelf and Figure S7 in Supporting Information S1 for the slope). The bimodality of the amplitude recovery arises from spurious detections often associated with days-scale to weeks-scale large pressure fluctuations that occur as part of the transition between winter and summer seasons. All correction techniques assessed in this study are based on least squares regression, so the offsets that result when the detector misses ramps will necessarily be accompanied by a comparable decrease elsewhere in the corrected pressure record to minimize the residuals. Figure 4b demonstrates this effect for the P_{ref} and no proxy corrections, though it occurs with varying frequency across all proxy corrections.

Whether on the shelf or slope, pressure data corrected with pressure-CEOFO seasonal corrections and P_{match} yield the best or among the best constraints on onset and amplitude (gray shading in Tables 1 and 2). The smallest SSEs that may be detected and characterized with these corrections have amplitudes of 4 cm on the shelf and 2 cm on the slope, comparing favorably with deformation amplitudes observed from SSEs in other studies. The difference in the threshold of detectability between shelf and slope is also roughly consistent with the ratio of post-correction RMS amplitudes between the two regions (Figure 6, Tables S3 and S4 in Supporting Information S1). Nearly all processing methods systematically underpredict ramp amplitudes and distributions are notably bimodal for small amplitudes (Figure 8), but the use of the pressure-CEOFO and P_{match} minimize these complications. Thus, our results provide evidence that CEOFs can be used to provide seasonal and higher-frequency corrections to seafloor pressure data without significantly impacting the determination of P_G amplitude, as compared to other seasonal correction methods. The timing accuracy that results from this preferred processing method should enable meaningful time-dependent SSE slip inversions, given the cm-scale SSE deformation amplitudes observed elsewhere. The potential to detect and characterize SSE deformation on the shelf is particularly important for the AACSE study area and much of Alaska, given the shelf's width of hundreds of kilometers and sparse onshore geodetic network. In a broader view, it is also significant in that it has generally been assumed previously that shelf pressure data are too noisy to be used in the detection of SSE deformation.

Longer deployments will help with correcting sensor drift and in the absence of known event timing, it would allow for sufficient data on either side of an SSE to adequately detect and characterize it. Going forward, extending

deployment duration to include multiple seasonal cycles would have multiple benefits for geodetic studies, to improve the preprocessing corrections for instrumental drift and seasonal variation. The former can be difficult to constrain due to the exponential component of unknown duration at the beginning of the deployment, which becomes increasingly problematic with increasing observation duration. Seasonal signals and interannual variability can be better characterized with each additional year of data. The latter has not been extensively studied to date, but may be significant noting that La Niña and El Niño have been observed to influence seafloor pressure records on the US west coast (e.g., Wilcock et al., 2021).

6. Conclusions

Our analyses quantify the patterns of significant coherence in seafloor pressure records from the Alaska margin over distances of hundreds of kilometers, controlled largely by location above or below the shelf break, and then secondarily by regional scale bathymetric features such as troughs and rises. We exploit this coherence to remove oceanographic signals from seafloor pressure records, thereby reducing the RMS of these records by as much as 83% on the shelf and 93% on the slope. The most effective approach to this involves first subtracting out the first CEOF of the combined pressure data set from either shelf or slope sites, and then using depth-matched differencing (the proxy P_{match}) to further correct the data. Most pressure records corrected in this way can be reduced to ≤ 1 cm RMS on the slope and ≤ 2 cm on the shelf. The separation and depth differences required to achieve those lowest RMS values are to first order consistent with what has been reported in Cascadia and Hikurangi margins, though the RMS values themselves are higher than what has been observed in those external locations.

We also demonstrate, through a synthetic detectability analysis, that the same combination of pressure-CEO and P_{match} corrections enable the greatest detectability of SSE deformation signals, allowing for statistically repeatable detection of 4 cm SSE signals on the shelf and 2 cm signals on the slope when no additional SSE constraints exist. Our analyses show that it is highly advantageous to have a priori information about event onset, perhaps provided by deformation observed on coastal GNSS stations. With known event timing, ramp amplitudes can be constrained to the ± 1 cm level on the shelf and the ± 0.5 cm level on the slope, while without this knowledge, ramps are systematically underpredicted and MADs are generally larger, particularly for small amplitude ramps.

Even with oceanographic signal corrections applied, significant residual pressure fluctuations occur at the transitions between winter and summer seasons and can be misidentified as SSE deformation, particularly when using an automated SSE detector. While collocated SSH data are highly predictive of these seasonal signals for stations on the shelf, they still fail to adequately predict other oceanographic signals and thus do not yield dramatic improvements to pressure RMS values or to SSE detectability. Nonetheless, this relationship warrants further exploration, as does the time-dependent and frequency-dependent correlation between seafloor temperature and pressure. Additional improvements to oceanographic corrections and SSE detectability are likely to arise from longer, multi-year observational records.

Our results demonstrate that seafloor pressure records properly corrected for oceanographic pressure effects may be powerful tools for identifying SSE and other small-amplitude transient tectonic deformation. In particular, we show that observations from the shelf, which have previously been neglected or simply not made, can be adequately corrected to reliably detect SSE deformation.

Data Availability Statement

The pressure and temperature data used in this study are available from the Incorporated Research Institutions for Seismology (IRIS) Data Management Center (ds.iris.edu/ds/nodes/dmc), archived under Network XO (2018–2019) (https://doi.org/10.7914/SN/XO_2018). Sea surface height data are available from the Copernicus Program (<http://marine.copernicus.eu/services-portfolio/access-to-products/>) archived as the product SEALEVEL-GLO-PHY-L4-MY-008-047 (<https://doi.org/10.48670/moi-00148>).

References

- Abers, G., Adams, A., Haeussler, P., Roland, E., Shore, P., Wiens, D., et al. (2019). Examining Alaska's earthquakes on land and sea. *Eos*, 100. <https://doi.org/10.1029/2019EO117621>
- Agata, R., Hori, T., Ariyoshi, K., & Ichimura, T. (2019). Detectability analysis of interplate fault slips in the Nankai subduction thrust using seafloor observation instruments. *Marine Geophysical Research*, 40(4), 453–466. <https://doi.org/10.1007/s11001-019-09380-y>

Acknowledgments

The authors thank David Schmidt and Parker MacCready of the University of Washington for their input and feedback on the detectability analysis and oceanographic interpretations, respectively. The authors also thank the Associate Editor, three anonymous reviewers, and Laura Wallace for their valuable feedback on the manuscript. This research was supported by NSF Grant OCE1951071. Any use of trade, firm, or product names is for descriptive purposes only and does not imply endorsement by the U.S. Government.

- Araki, E., Saffer, D. M., Kopf, A. J., Wallace, L. M., Kimura, T., Machida, Y., et al. (2017). Recurring and triggered slow-slip events near the trench at the Nankai Trough subduction megathrust. *Science*, 356(6343), 1157–1160. <https://doi.org/10.1126/science.aan3120>
- Ariyoshi, K., Nakata, R., Matsuzawa, T., Hino, R., Hori, T., Hasegawa, A., & Kaneda, Y. (2014). The detectability of shallow slow earthquakes by the Dense Oceanfloor Network system for Earthquakes and Tsunamis (DONET) in Tonankai district, Japan. *Marine Geophysical Research*, 35(3), 295–310. <https://doi.org/10.1007/s11001-013-9192-6>
- Baba, T., Hirata, K., Hori, T., & Sakaguchi, H. (2006). Offshore geodetic data conducive to the estimation of the afterslip distribution following the 2003 Tokachi-oki earthquake. *Earth and Planetary Science Letters*, 241(1–2), 281–292. <https://doi.org/10.1016/j.epsl.2005.10.019>
- Barcheck, G., Abers, G. A., Adams, A. N., Bécel, A., Collins, J., Gaherty, J. B., et al. (2020). The Alaska amphibious community seismic experiment. *Seismological Research Letters*, 91(6), 3054–3063. <https://doi.org/10.1785/0220200189>
- Brown, J. R., Prejean, S. G., Beroza, G. C., Gomberg, J. S., & Haussler, P. J. (2013). Deep low-frequency earthquakes in tectonic tremor along the Alaska-Aleutian subduction zone. *Journal of Geophysical Research: Solid Earth*, 118(3), 1079–1090. <https://doi.org/10.1029/2012JB009459>
- Capotondi, A., Combes, V., Alexander, M. A., Di Lorenzo, E., & Miller, A. J. (2009). Low-frequency variability in the Gulf of Alaska from coarse and eddy-permitting ocean models. *Journal of Geophysical Research*, 114(C1), C01017. <https://doi.org/10.1029/2008JC004983>
- Coyle, K. O., Hermann, A. J., & Hopcroft, R. R. (2019). Modeled spatial-temporal distribution of productivity, chlorophyll, iron and nitrate on the northern Gulf of Alaska shelf relative to field observations. *Deep Sea Research Part II: Topical Studies in Oceanography*, 165, 163–191. <https://doi.org/10.1016/j.dsrr.2019.05.006>
- Crowell, B. W., & Melgar, D. (2020). Slipping the Shumagin gap: A kinematic coseismic and early afterslip model of the Mw 7.8 Simeonof Island, Alaska, earthquake. *Geophysical Research Letters*, 47(19), 1–7. <https://doi.org/10.1029/2020GL090308>
- Davies, J., Sykes, L., House, L., & Jacob, K. (1981). Shumagin Seismic Gap, Alaska Peninsula: History of great earthquakes, tectonic setting, and evidence for high seismic potential. *Journal of Geophysical Research*, 86(B5), 3821. <https://doi.org/10.1029/JB086iB05p03821>
- Davis, E. E., Villinger, H., & Sun, T. (2015). Slow and delayed deformation and uplift of the outermost subduction prism following ETS and seismogenic slip events beneath Nicoya Peninsula, Costa Rica. *Earth and Planetary Science Letters*, 410, 117–127. <https://doi.org/10.1016/j.epsl.2014.11.015>
- Dixon, T. H., Jiang, Y., Malservisi, R., McCaffrey, R., Voss, N., Protti, M., & Gonzalez, V. (2014). Earthquake and tsunami forecasts: Relation of slow slip events to subsequent earthquake rupture. *Proceedings of the National Academy of Sciences of the United States of America*, 111(48), 17039–17044. <https://doi.org/10.1073/pnas.1412299111>
- Dobashi, Y., & Inazu, D. (2021). Improving detectability of seafloor deformation from bottom pressure observations using numerical ocean models. *Frontiers of Earth Science*, 8, 1–16. <https://doi.org/10.3389/feart.2020.598270>
- Elliott, J. L., Grapenthin, R., Parameswaran, R. M., Xiao, Z., Freymueller, J. T., & Fusco, L. (2022). Cascading rupture of a megathrust. *Science Advances*, 8(18), eabm4131. <https://doi.org/10.1126/sciadv.abm4131>
- Foreman, M. G. G., Crawford, W. R., Cherniawsky, J. Y., Henry, R. F., & Tarbotton, M. R. (2000). A high-resolution assimilating tidal model for the northeast Pacific Ocean. *Journal of Geophysical Research: Oceans*, 105(C12), 28629–28651. <https://doi.org/10.1029/1999JC000122>
- Fournier, T. J., & Freymueller, J. T. (2007). Transition from locked to creeping subduction in the Shumagin region, Alaska. *Geophysical Research Letters*, 34(6), L06303. <https://doi.org/10.1029/2006GL029073>
- Fredrickson, E. K., Wilcock, W. S. D., Schmidt, D. A., MacCready, P., Roland, E. C., Kurapov, A. L., et al. (2019). Optimizing sensor configurations for the detection of slow slip earthquakes in seafloor pressure records, using the Cascadia Subduction Zone as a case study. *Journal of Geophysical Research: Solid Earth*, 124(12), 13504–13531. <https://doi.org/10.1029/2019jb018053>
- Gomberg, J., Hautala, S., Johnson, P., & Chiswell, S. (2019). Separating sea and slow slip signals on the seafloor. *Journal of Geophysical Research: Solid Earth*, 124(12), 13486–13503. <https://doi.org/10.1029/2019JB018285>
- He, B., Wei, M., Watts, D. R., & Shen, Y. (2020). Detecting slow slip events from seafloor pressure data using machine learning. *Geophysical Research Letters*, 47(11), 1–8. <https://doi.org/10.1029/2020GL087579>
- He, B., Wei, X., Wei, M., Shen, Y., & Alvarez, M. (2021). A likely slow slip event detected by seafloor pressure data offshore southwest Alaska in 2018. In *AGU fall Meeting Abstracts 2021*, 0544A-06.
- Hermann, A. J., Hinckley, S., Dobbins, E. L., Haidvogel, D. B., Bond, N. A., Mordy, C., et al. (2009). Quantifying cross-shelf and vertical nutrient flux in the Coastal Gulf of Alaska with a spatially nested, coupled biophysical model. *Deep Sea Research Part II: Topical Studies in Oceanography*, 56(24), 2474–2486. <https://doi.org/10.1016/j.dsrr.2009.02.008>
- Hino, R., Inazu, D., Ohta, Y., Ito, Y., Suzuki, S., Iinuma, T., et al. (2014). Was the 2011 Tohoku-Oki earthquake preceded by aseismic preslip? Examination of seafloor vertical deformation data near the epicenter. *Marine Geophysical Research*, 35(3), 181–190. <https://doi.org/10.1007/s11001-013-9208-2>
- Hughes, C. W., & Meredith, M. P. (2006). Coherent sea-level fluctuations along the global continental slope. *Philosophical Transactions of the Royal Society A: Mathematical, Physical & Engineering Sciences*, 364(1841), 885–901. <https://doi.org/10.1098/rsta.2006.1744>
- Hughes, C. W., Williams, J., Blaker, A., Coward, A., & Stepanov, V. (2018). A window on the deep ocean: The special value of ocean bottom pressure for monitoring the large-scale, deep-ocean circulation. *Progress in Oceanography*, 161, 19–46. <https://doi.org/10.1016/j.pocean.2018.01.011>
- Inoue, T., Ito, Y., Wallace, L. M., Yoshikawa, Y., Inazu, D., Garcia, E. S. M., et al. (2021). Water depth dependence of long-range correlation in nontidal variations in seafloor pressure. *Geophysical Research Letters*, 48(8), e2020GL092173. <https://doi.org/10.1029/2020GL092173>
- Ito, Y., Hino, R., Kido, M., Fujimoto, H., Osada, Y., Inazu, D., et al. (2013). Episodic slow slip events in the Japan subduction zone before the 2011 Tohoku-Oki earthquake. *Tectonophysics*, 600, 14–26. <https://doi.org/10.1016/j.tecto.2012.08.022>
- Itoh, Y., Nishimura, T., Ariyoshi, K., & Matsumoto, H. (2019). Interplate slip following the 2003 Tokachi-oki earthquake from ocean bottom pressure gauge and land GNSS data. *Journal of Geophysical Research: Solid Earth*, 124(4), 4205–4230. <https://doi.org/10.1029/2018JB016328>
- Johnson, H. P., Gomberg, J. S., Hautala, S. L., & Salmi, M. S. (2017). Sediment gravity flows triggered by remotely generated earthquake waves. *Journal of Geophysical Research: Solid Earth*, 122(6), 4584–4600. <https://doi.org/10.1002/2016JB013689>
- Kawaguchi, K., Kaneko, S., Nishida, T., & Komine, T. (2015). Construction of the DONET real-time seafloor observatory for earthquakes and tsunami monitoring. In *Seafloor Observatories* (pp. 211–228). https://doi.org/10.1007/978-3-642-11374-1_10
- Ladd, C., Mordy, C. W., Kachel, N. B., & Staben, P. J. (2007). Northern Gulf of Alaska eddies and associated anomalies. *Deep-Sea Research I*, 54(4), 487–509. <https://doi.org/10.1016/j.dsr.2007.01.006>
- Li, S., & Freymueller, J. T. (2018). Spatial variation of slip behavior beneath the Alaska Peninsula along Alaska-Aleutian subduction zone. *Geophysical Research Letters*, 45(8), 3453–3460. <https://doi.org/10.1002/2017GL076761>
- Luther, D. S., Chave, A. D., Filloux, J. H., & Spain, P. F. (1990). Evidence for local and nonlocal barotropic responses to atmospheric forcing during BEMPEX. *Geophysical Research Letters*, 17(7), 949–952. <https://doi.org/10.1029/GL017i007p00949>

- Muramoto, T., Ito, Y., Inazu, D., Wallace, L. M., Hino, R., Suzuki, S., et al. (2019). Seafloor crustal deformation on ocean bottom pressure records with nontidal variability corrections: Application to Hikurangi Margin, New Zealand. *Geophysical Research Letters*, 46(1), 303–310. <https://doi.org/10.1029/2018GL080830>
- Ozawa, S., Suito, H., & Tobita, M. (2007). Occurrence of quasi-periodic slow-slip off the east coast of the Boso peninsula, central Japan. *Earth Planets and Space*, 59(12), 1241–1245. <https://doi.org/10.1186/BF03352072>
- Polster, A., Fabian, M., & Villingen, H. (2009). Effective resolution and drift of paroscientific pressure sensors derived from long-term seafloor measurements. *Geochemistry, Geophysics, Geosystems*, 10(8), Q08008. <https://doi.org/10.1029/2009GC002532>
- Radiguet, M., Perfettini, H., Cotte, N., Gualandri, A., Valette, B., Kostoglodov, V., et al. (2016). Triggering of the 2014 Mw 7.3 Papanoa earthquake by a slow-slip event in Guerrero, Mexico. *Nature Geoscience*, 9(11), 829–833. <https://doi.org/10.1038/ngeo2817>
- Reed, R. K., & Stabeno, P. J. (1989). Recent observations of variability in the path and vertical structure of the Alaskan Stream. *Journal of Physical Oceanography*, 19(10), 1634–1642. [https://doi.org/10.1175/1520-0485\(1989\)019<1634:rovit>2.0.co;2](https://doi.org/10.1175/1520-0485(1989)019<1634:rovit>2.0.co;2)
- Roussel, B., Fu, Y., Bartlow, N., & Bürgmann, R. (2019). Weeks-long and years-long slow slip and tectonic tremor episodes on the south-central Alaska megathrust. *Journal of Geophysical Research: Solid Earth*, 124(12), 13392–13403. <https://doi.org/10.1029/2019JB018724>
- Ruiz, S., Métois, M., Fuenzalida, A., Ruiz, J., Leyton, F., Grandin, R., et al. (2014). Intense foreshocks and a slow-slip preceded the 2014 Iquique Mw 8.1 earthquake. *Science*, 345(6201), 1165–1169. <https://doi.org/10.1126/science.1256074>
- Siegismund, F., Romanova, V., Köhl, A., & Stammer, D. (2011). Ocean bottom pressure variations estimated from gravity, nonsteric sea surface height and hydrodynamic model simulations. *Journal of Geophysical Research: Oceans*, 116(C7), 2010JC006727. <https://doi.org/10.1029/2010JC006727>
- Stabeno, P. J., Bell, S., Cheng, W., Danielson, S., Kachel, N. B., & Mordy, C. W. (2016). Long-term observations of Alaska Coastal Current in the northern Gulf of Alaska. *Deep-Sea Research Part II Topical Studies in Oceanography*, 132, 24–40. <https://doi.org/10.1016/j.dsr2.2015.12.016>
- Stabeno, P. J., Bond, N. A., Hermann, A. J., Kachel, N. B., Mordy, C. W., & Overland, J. E. (2004). Meteorology and oceanography of the Northern Gulf of Alaska. *Continental Shelf Research*, 24(7–8), 859–897. <https://doi.org/10.1016/j.csr.2004.02.007>
- Stabeno, P. J., Bond, N. A., Kachel, N. B., Ladd, C., Mordy, C. W., & Strom, S. L. (2016). Southeast Alaskan shelf from southern tip of Baranof Island to Kayak Island: Currents, mixing and chlorophyll-a. *Deep-Sea Research Part II Topical Studies in Oceanography*, 132, 6–23. <https://doi.org/10.1016/j.dsr2.2015.06.018>
- Stabeno, P. J., & Hristova, H. G. (2014). Observations of the Alaskan Stream near Samalga Pass and its connection to the Bering Sea: 2001–2004. *Deep-Sea Research Part I: Oceanographic Research Papers*, 88, 30–46. <https://doi.org/10.1016/j.dsr.2014.03.002>
- Suzuki, K., Araki, E., & Takahashi, N. (2018). Detectability of crustal deformation by using ocean bottom pressure gauges deployed to DONET system. 2018 OCEANS - MTS/IEEE Kobe Techno-Oceans, OCEANS - Kobe 2018, 12–15. <https://doi.org/10.1109/OCEANSKOBE.2018.8559470>
- Taburet, G., Sanchez-Roman, A., Ballarotta, M., Pujol, M.-I., Legeais, J.-F., Fournier, F., et al. (2019). DUACS DT2018: 25 years of reprocessed sea level altimetry products. *Ocean Science*, 15(5), 1207–1224. <https://doi.org/10.5194/os-15-1207-2019>
- Thomson, R. E., & Emery, W. J. (2014). *Data analysis methods in physical oceanography*. Elsevier. <https://doi.org/10.1016/C2010-0-66362-0>
- Todd, E. K., Schwartz, S. Y., Mochizuki, K., Wallace, L. M., Sheehan, A. F., Webb, S. C., et al. (2018). Earthquakes and tremor linked to seamount subduction during shallow slow-slip at the Hikurangi Margin, New Zealand. *Journal of Geophysical Research: Solid Earth*, 123(8), 6769–6783. <https://doi.org/10.1029/2018JB016136>
- Toomey, D. R., Allen, R. M., Barclay, A. H., Samuel, W., Bromirski, P. D., Carlson, R. L., et al. (2014). The Cascadia Initiative: A sea change in seismological studies of subduction zones. *Oceanography*, 27(2), 138–150. <https://doi.org/10.5670/oceanog.2014.49>
- Vallée, M., Nocquet, J. M., Battaglia, J., Font, Y., Segovia, M., Régnier, M., et al. (2013). Intense interface seismicity triggered by a shallow slow-slip event in the Central Ecuador subduction zone. *Journal of Geophysical Research: Solid Earth*, 118(6), 2965–2981. <https://doi.org/10.1002/jgrb.50216>
- Wallace, L. M., & Beavan, J. (2010). Diverse slow-slip behavior at the Hikurangi subduction margin, New Zealand. *Journal of Geophysical Research: Solid Earth*, 115(12), 1–20. <https://doi.org/10.1029/2010JB007717>
- Wallace, L. M., Webb, S. C., Ito, Y., Mochizuki, K., Hino, R., Henrys, S., et al. (2016). Slow-slip near the trench at the Hikurangi subduction zone, New Zealand. *Science*, 352(6286), 701–704. <https://doi.org/10.1126/science.aaf2349>
- Wang, D.-P., & Mooers, C. N. K. (1976). Coastal-trapped waves in a continuously stratified ocean. *Journal of Physical Oceanography*, 6(6), 853–863. [https://doi.org/10.1175/1520-0485\(1976\)006<0853:CTWIAC>2.0.CO;2](https://doi.org/10.1175/1520-0485(1976)006<0853:CTWIAC>2.0.CO;2)
- Warren, B. A., & Owens, W. B. (1988). Deep currents in the central subarctic Pacific Ocean. *Journal of Physical Oceanography*, 18(4), 529–551. [https://doi.org/10.1175/1520-0485\(1988\)018<0529:DCITC>2.0.CO;2](https://doi.org/10.1175/1520-0485(1988)018<0529:DCITC>2.0.CO;2)
- Watts, D. R., Wei, M., Tracey, K. L., Donohue, K. A., & He, B. (2021). Seafloor geodetic pressure measurements to detect shallow slow-slip events: Methods to remove contributions from ocean water. *Journal of Geophysical Research: Solid Earth*, 126(4), 1–15. <https://doi.org/10.1029/2020JB020065>
- Wilcock, W. S. D., Manalang, D. A., Fredrickson, E. K., Harrington, M. J., Cram, G., Tilley, J., et al. (2021). A thirty-month seafloor test of the A-0-A method for calibrating pressure gauges. *Frontiers of Earth Science*, 8, 600671. <https://doi.org/10.3389/feart.2020.600671>
- Woods, K., Wallace, L. M., Webb, S. C., Ito, Y., Savage, M. K., Chadwell, C. D., et al. (2020). Updip migration of slow-slip revealed through seafloor geodesy during 2019 East Coast slow-slip at the Hikurangi Margin, New Zealand. In *AGU Fall Meeting Abstracts 2020*, 0222-04.
- Woods, K., Webb, S. C., Wallace, L. M., Ito, Y., Collins, C., Palmer, N., et al. (2022). Using seafloor geodesy to detect vertical deformation at the Hikurangi subduction zone: Insights from self-calibrating pressure sensors and ocean general circulation models. *Journal of Geophysical Research: Solid Earth*, 127(12), 1–22. <https://doi.org/10.1029/2022JB023989>
- Wunsch, C. (2016). Global ocean integrals and means, with trend implications. *Annual Review of Marine Science*, 8, 1–33. <https://doi.org/10.1146/annurev-marine-122414-034040>